TECHNISCHE UNIVERSITÄT WIEN

ACIN AUTOMATION & CONTROL INSTITUTE INSTITUT FÜR AUTOMATISIERUNGS- & REGELUNGSTECHNIK

Dual stage-controlled robotic system for precise inline 3D measurements on moving objects

DIPLOMARBEIT

Ausgeführt zum Zwecke der Erlangung des akademischen Grades eines
Diplom-Ingenieurs (Dipl.-Ing.)

unter der Leitung von

Univ.-Prof. Dr.sc.techn. Georg Schitter

Dipl.-Ing. Daniel Wertjanz
Dipl.-Ing. Peter Gsellmann

eingereicht an der
Technischen Universität Wien
Fakultät für Elektrotechnik und Informationstechnik
Institut für Automatisierungs- und Regelungstechnik

von

Matthias Laimer, BSc.
Matrikelnummer: 01618525

Wien, im Juli 2022

Advanced Mechatronic Systems Group
GuSShausstrasse 27-29, A-1040 Wien, Internet: http://www.acin.tuwien.ac.at

Acknowledgements

I would like to thank all those who accompanied me on the path of my studies and contributed to the successful realisation of my master thesis.

First and foremost, I would like to express my deepest gratitude to my daily supervisor, Dipl.-Ing. Daniel Wertjanz, for his tireless effort, offering his support, and always sharing his time if needed for inspiring discussions. I would like to extend my sincere thanks to my further supervisor, Dipl.-Ing. Peter Gsellmann, for offering me his advice and sharing his knowledge over the whole course of this thesis. I am also grateful to Univ.-Prof. Dr.sc.techn. Georg Schitter, for the opportunity to write this thesis and his guidance. Thanks should also go to all my colleagues and friends at university but of course also to all the other members of the Advanced Mechatronic Systems (AMS) group for the fruitful discussions and creating this comfortable and pleasant working atmosphere.

Finally, my deepest gratitude goes to my parents Manuela and Elmar, and my sister Carina. I could not have undertaken this journey without their unfailing support and always putting their faith in me. Special thanks also go to my girlfriend Alexandra for her never-ending patience and encouraging conversations during the last years but especially throughout the conducting of this thesis.

Thank you!

Abstract

To accomplish the demands for increasing product quality, an efficient 100 % quality control for products with structures on the single- or even sub-micrometre range is desired. Robotic inline 3D measurement systems play a particularly important role in this context, as they can enable the flexible sample inspection at arbitrary measurement spots. However, as the positioning precision of industrial robots as well as environmental disturbances cause relative motion between the measurement tool on the industrial robot and the sample in the range of several tens of micrometres, the integration of robotic 3D measurement systems with sub-micrometre precision into an industrial production line is considered as a major challenge.
Therefore, a robotic 3D measurement system including an electromagnetically levitated sample tracking measurement platform to maintain constant position of the integrated 3D measurement tool relative to a sample has been proposed recently. In this thesis, the provided robotic 3D measurement system is advanced towards precision measurements on moving objects by means of a dual stage-control concept, such as required for future inline applications. The relative position between the sample tracking measurement platform and the industrial robot measured by the internal position sensor system is used to precisely reposition the industrial robot, maintaining the measurement platform within its actuation range. A sophisticated control architecture combining feedback control as well as the conveyor velocity as *a priori* knowledge in a feedforward approach is designed and evaluated.
The performance of the dual stage-controlled robotic system is identified by tracking a moving sample on a conveyor system. Residual sample tracking errors of 486 nm in motion and 167 nm in the vertical direction at a sample velocity of 10 mm/s are achieved. With the moving sample being actively tracked, the system is capable of performing 3D measurements with resolutions down to 620 nm, achieving sub-micrometre precision.

Zusammenfassung

Um den Forderungen der steigenden Produktqualität gerecht zu werden, ist eine 100 %-ige Qualitätskontrolle von Produkten mit Strukturen im einstelligen bzw. Submikrometerbereich unabdingbar. In diesem Zusammenhang spielen robotergestützte Inline-3D-Messsysteme eine wichtige Rolle. Sie ermöglichen die flexible Prüfung an beliebigen Messpunkten an dem zu messenden Objekt. Da jedoch die limitierte Positioniergenauigkeit von Industrierobotern sowie Umgebungsstörungen eine Relativbewegung in der Größenordnung mehrerer zehn Mikrometern zwischen dem Messsystem und dem -objekt verursachen, gilt die Integration robotergestützter 3D-Messsysteme mit Auflösungen im Submikrometerbereich in industriellen Fertigungsanlagen als große Herausforderung.
Kürzlich wurde ein robotergestütztes 3D-Messsystem mit einer elektromagnetisch-aktuierten, schwebenden Messplattform präsentiert, um die Position des integrierten Messsystems relativ zu dem -objekt konstant zu halten. Ziel dieser Arbeit ist das vorgestellte roboterbasierte 3D-Messsystem durch ein zweistufiges Regelungsskonzept für Präzisionsmessungen an bewegten Objekten weiterzuentwickeln. Die vom internen Positionssensorsystem gemessene Relativposition zwischen der Messplattform und dem Industrieroboter wird hierbei zur präzisen Repositionierung des Industrieroboters verwendet, um somit die Messplattform innerhalb ihres mechanischen Stellbereichs zu halten.
Die Performanz des zweistufig geregelten Robotersystems wird durch das aktive Nachführen des Messystems entlang der Bewegung des Messobjekts auf einer Förderanlage ermittelt. Es werden Restfehler bei der aktiven Verfolgung von 486 nm in bewegungs- und 167 nm in der vertikalen Richtung bei einer Messobjektgeschwindigkeit von 10 mm/s erreicht. Während der aktiven Messobjektsverfolgung ist das integrierte 3D-Messsystem in der Lage Messungen mit einer Auflösung im Submikrometerbereich von bis zu 620 nm durchzuführen.

Contents

List of Figures

List of Tables

CHAPTER 1

Introduction

Modern industrial manufacturing is facing new challenges due to ongoing global trends towards flexibility, resource efficiency, high quality and modular production. As a result, particular attention is paid to the development of versatile measurement systems, focusing on deploying new measurement strategies directly within the production line [1–3].

1.1 Motivation

The desired 100 % quality control of industrially produced goods to further improve the production efficiency is one of the appointed targets of future manufacturing [4, 5]. Among others, inline measurement systems are seen as a key factor to accomplish these objectives. The main idea of this approach is to deploy the measurement systems directly in the production process, avoiding the undesirable un-/loading step of the produced goods, and to further enable fully monitoring of the process step [2]. Earlier detection of defects in the manufactured products or recognition of problems in the production process itself are just few of the benefits of inline measurement systems. However, as *"There is no such thing as a free lunch" (Robert A. Heinlein, 1966, p.129)*, more effort has to be put in the development of new measurement systems, with special focus on the fundamental trade-off between the system requirements such as compactness, robustness, preciseness, flexibility and speed [4], with applications ranging from the semiconductor to the automotive and consumer electronics sector [6–9].

Nevertheless, the integration of high precision measurement tools (MTs) directly into the vibration-prone environment of an industrial production line is considered as a major challenge. In today's production lines, industrial robots (IRs) in combination with high precision MTs are deployed to enable highly flexible positioning of the MT at arbitrary measurement locations or to extend its measurement range [10–12]. However, modern IRs are designed for executing repetitive operations, where motions with high repeatability between taught points are required. The position accuracy of modern IRs varies between tens of micrometres up to millimetres [13]. Therefore, IRs themselves are not suitable to position a MT with single- or submicrometre precision. The resulting relative motion between the MT and the sample surface would lead to motion blur in the measurement result, impairing the overall measurement performance [14, 15].

The lack of IRs providing the required positioning accuracy is not the only challenge for the integration of precision measurements directly in the production line. The presence of environmental disturbances is a further source of relative motion between the MT and the sample, which leads to motion blur, limiting the targeted measurement resolutions. In order to compensate this relative motion, active sample tracking approaches have been excessively investigated in recent years, where the use of the magnetic levitation (MAGLEV) actuation principles show promising progress [16–19]. In this approach, the MT is mounted to a measurement platform (MP), which establishes the desired contactless stiff link between the MT and the sample surface by means of feedback control [20]. In this way, disturbance-induced relative motion is actively compensated. However, these systems are often limited in the actuation range, that leads to a constrained measurement area on the sample surface [21].

In a next step towards inline 3D measurements on moving objects with submicrometre positioning precision, IRs in combination with the aforementioned active sample tracking measurement module constitutes as a viable approach [22]. Thus, by the utilization of dual stage principles, 3D measurements on the submicrometre scale can be enabled, combining the high precision sample tracking of the measurement module with the coarse but long-range positioning capability of IRs establishing the desired stiff link between the measurement tool and the moving sample [23–25].

1.2 Research goals and objectives

Motivated by the future application of robotic inline 3D measurements on moving objects with submicrometre precision, this thesis aims to design and implement a

dual stage-controlled robotic system, which is capable of actively tracking a sample on a conveyor system, and at the same time performing precision 3D measurements on the sample surface. Therefore, the robotic 3D measurement system [20] is provided as a basis. Up to this point, the IR is solely used to statically position the active sample tracking 3D measurement module with respect to a sample surface. The integrated MP provides an actuation range of $\pm 175\,\mu m$ and $\pm 3\,mrad$ for the translational and rotational degree of freedoms (DoFs), respectively. However, the entire system lacks the ability to actively track the motion of a sample on the large scale, such as being transported by an industrial conveyor system.

Besides tracking sensors (TSs), which measure the MP position relative to the sample surface, internal position sensors (IPSs) are used to detect the relative motion performed by the MP with respect to the robot arm. While the sample is being actively tracked by the MP lab-like conditions for the 3D measurement tool are established. For that reason, the IPS signal may be used in a dual stage control approach to precisely reposition the IR such that the MP is maintained within its limited actuation range.

With an eye towards the targeted application, a suitable communication interface between the sample tracking 3D measurement module and the robot control has to be selected to enable a precise IR repositioning in real time. Moreover, an industrial-like conveying system is required for evaluating the performance of the robotic inline 3D measurement system on moving objects. Given the limited translational range of about 0.7 m of the provided robotic system prototype and typical process cycle times in the automotive industry of about 70 s [26], sample motions with speeds of up to 10 mm/s are aimed to be robustly tracked. Residual tracking errors on the sub-micrometre scale are targeted, while performing 3D measurements with sub-micrometre precision on the long-range moving sample.

Considering these aspects, the main objectives of this thesis are defined as follows:

- Establishment of a real-time communication between the industrial robot and the sample tracking 3D measurement module.
- Development and implementation of a dual stage-control architecture for the real-time repositioning of the IR.
- Evaluation of the robotic inline 3D measurement system performance in an industrial-like, vibration-prone environment.

1.3 Thesis outline

The remainder of this thesis is structured as follows. In a first step, Chapter 2 discusses state-of-the-art measurement architectures in industrial production, robotic inline measurement solutions, high precision active sample tracking measurement modules and motion control strategies. Chapter 3 gives an overview of the system concept. In Chapter 4 the soft- and hardware components used in this system are introduced. The pose-dependent dynamics of the IR are identified in Chapter 5. Based on these results a dual stage control for precisely repositioning the IR is designed. Chapter 6 evaluates the long-range sample tracking performance as well as the 3D imaging performance on a moving sample being transported by a conveyor system. A summary of the results and findings in Chapter 7 concludes this thesis.

CHAPTER 2

State of the Art

This chapter presents different measurement strategies applied in industrial manufacturing plants as well as an analysis of their benefits and drawbacks. In this relation, the focus is on robot-based inline measurement systems, emphasizing the importance of active sample tracking approaches to compensate environmental disturbances. Furthermore, a discussion on the fundamental aspects of different motion control strategies is given.

2.1 From off-/online to advanced robotic inline measurement applications

In the following, the different concepts of sample inspection in industrial manufacturing are presented. Furthermore, advanced robotic inline measurement systems as well as the related limitations regarding measurement precision are discussed.

2.1.1 Measurement architectures in industrial manufacturing

The trend towards production that can be flexibly and quickly adapted to the demands of customers and the market is unbroken [27]. In order to meet those demands, new and advanced measurement systems in the industrial production are needed. The integration of the measurement system, leading to a reduction of the measurement time, is seen as one of the key factors in order to enable high

precision and flexible production lines [2]. These developments have led to a strong push in the scientific field of measurement technologies, with its major challenges to be fast, accurate, robust and versatile [27]. In the following, the concept of inline metrology is explained in more detail with a comparison of conventional measurement strategies, highlighting the benefits of inline metrology and its upcoming challenges.

Nowadays, broadly conventional measurement concepts, stated as off-/online metrology, are used for quality control in the production line. The strategies illustrated in Figure 2.1a and 2.1b have in common that samples have to be unloaded after a production step and to perform the targeted quality measurement in a special, often locally separated, lab environment, which is isolated from external disturbances. In comparison, to offline measurement systems, online metrology uses the measurement outputs to adapt the production step, if necessary.
As a result, the targeted 100 % quality control is not achievable using these concepts [4]. In contrast, the idea of inline metrology is to integrate the measurement equipment directly in the production process. In this way, a 100 % quality control, i.e., the inspection of all produced goods, is achievable (see Figure 2.1c). Furthermore, the acquisition of the measured data allows to identify failures in the production process at earlier stages, whereby countermeasures can be set faster [4].

2.1.2 Robotic inline measurement systems

Nowadays, the automotive industry relies mainly on offline measurement concepts to inspect the produced parts. For that reason, coordinate measuring machines (CMMs) are playing an important role in the quality assessment, due to their high accuracy and repeatability, as well as the availability of international standards for calibration and measurement uncertainties [26, 28]. However, on the way to 100 % quality control without sacrificing production efficiency and throughput, the use of CMMs is not suitable. Reasons for this are the need of undesired un-/loading steps from the assembly line, the mechanical clamping of the manufactures parts in a measurement fixture by an operator, increasing measurement time with the complexity of the sample structure, since several alignment steps relative to the CMM might be needed, and slow measuring speed because of the single-point measurement technique [26, 28, 29].

The direct application of industrial robots (IRs) equipped with a precision measurement tool (MT) in the production line is seen to fill this gap, due to the high flexibility given by the IR's workspace to locate the MT at arbitrary measurement locations and to extend its measurement range, which allows to inspect complex structures [30]. Since cycle times of 70 s and less are common for production steps

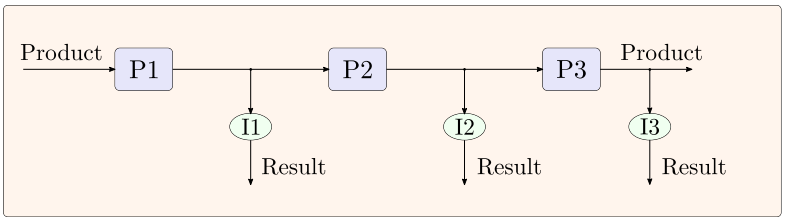

(a) Offline

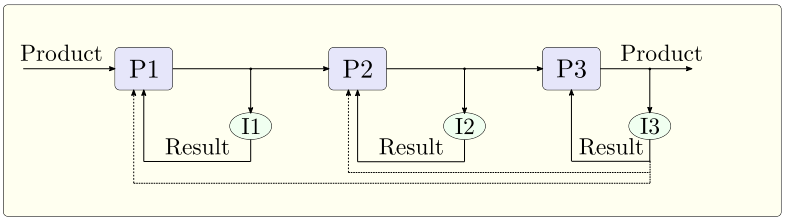

(b) Online

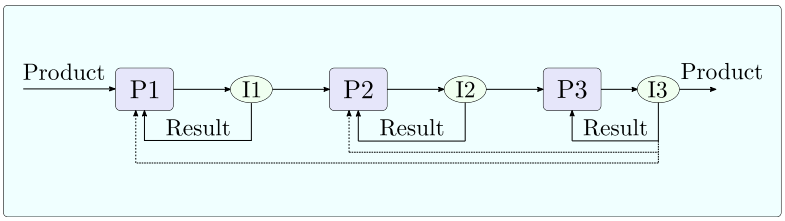

(c) Inline

Figure 2.1: Comparison of different sample inspection strategies in the industrial manufacturing. P1 to P3 indicate production steps and I1 to I3 mark inspection tasks. (a) shows an offline metrology application in which after each production step the sample is unloaded and measured separately from the production line. The result has no impact on the production process. In comparison, online metrology (b) uses the measurement result to adapt the process, if necessary. Inline metrology (c) deploys the measurement system directly into the production process, which allows to fully monitor the sample and the process [4].

in the automotive industry, the time needed for the robotic inline measurement has to be on the same scale, in order to achieve the desired high throughput and efficiency [26]. Figure 2.2 shows the ABIS II (Carl Zeiss Optotechnik, GmbH, Neubeuern, Deutschland), which allows to inspect the surface quality of body parts by using an optical 3D sensor with measurement times of few seconds and resolutions down to 10 µm. As illustrated in this figure, several of these systems can collaborate on one part at the same time, which further increases the efficiency. Additional state-of-the-art robotic inline measurement systems, as described in [32] and [33], are using laser sensors, which allow a non-tactile 3D inspection of surfaces, with both systems achieving resolutions down to 50 µm.

Figure 2.2: Collaboration of several ABIS II for car body surface inspection directly at the assembly line. The optical 3D sensors are mounted to the IRs, which allows to perform inspection tasks within few seconds with resolutions down to 10 µm [31].

2.1.3 Challenges and limitations

However, resolutions on the single or even sub-micrometre scale are hardly achievable, by using IRs directly equipped with precision MTs. The reason for this is the limited position accuracy of IRs, which is typically in the range of several tens of micrometres up to millimetres [13, 34]. The resulting relative motion between the MT and the sample leads to motion blur, corrupting measurements on the submicro or even microscale [15]. Since the main application of IRs in modern production lines is to perform repetitive operations, such as welding the same spots on each car body produced [34, 35], a high repeatability is required for the motion between taught points [36]. Different influences can be addressed that reduces the robot accuracies, which can be grouped into geometrical and non-geometrical errors [37]. Geometric errors are a result, caused by imperfections in the manufacturing process of the IR [36], but also from the equipped payload at the end effector, which leads to joint deformations [38], resulting in an inaccurate positioning of the tool center point (TCP). As indicated, a TCP misalignment is not measurable by the IR encoder system for a deformed joint, as the position calculation solely relies on the measured joint angles. For that reason, Abbe errors, as schematically shown for one joint in Figure 2.3, are seen as the worst type of geometrical errors, since angular

errors get amplified [36]. The group of non-geometrical errors consider further

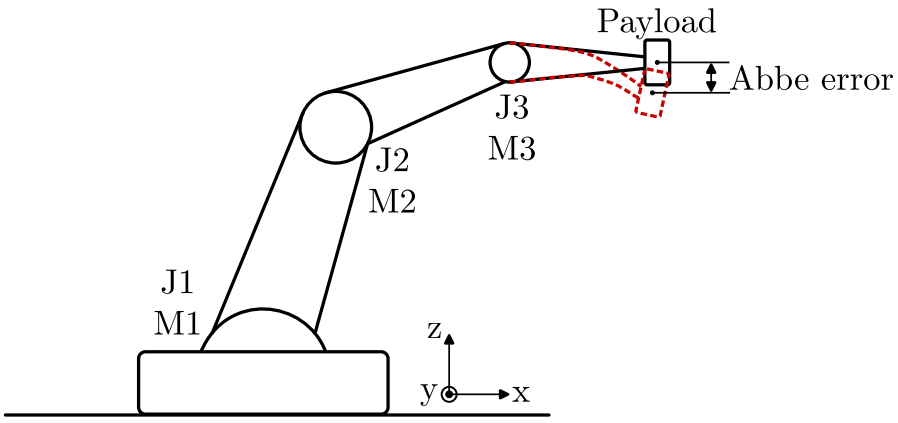

Figure 2.3: Illustration of the Abbe error for a 3 degree of freedom (DoF) IR schematically shown for the last joint J3 with the motor torque M3. Due to the finite stiffness of the mechanical IR components, a payload fixed to the IR leads to a deformation of the joint, which is not detected by the IR encoders, resulting in an inaccurate positioning of the IR's TCP [36].

influences, such as thermal errors, which lead to an expansion of materials, dynamic errors, due to the robot motion, and system errors, such as sensor inaccuracies [34, 36]. Different calibration methods have been developed to compensate geometrical and non-geometrical errors. A detailed description of these concepts would go beyond the scope of this thesis, but can be found in [22, 34, 37, 39].

However, the limited positioning accuracy of IRs is not the only source for motion blur in the resulting measurement. The presence of external disturbances in production lines, such as environmental vibrations caused by running machines etc., leads to additional relative motion between the sample and the MT, which further limits the achievable resolution [15]. In Figure 2.4, typical disturbance sources ocurring in a multilevel building are shown. As can be seen, most of the disturbances show a frequency range of up to 200 Hz [40], with pre-dominant components in the lower range up to 80 Hz [41].

Summing up, state-of-the-art robotic inline measurement systems achieve resolutions down to several tens of micrometers, limited by the positioning accuracy of IRs and environmental disturbances in an industrial production line, both causing motion blur in the targeted precision measurement.

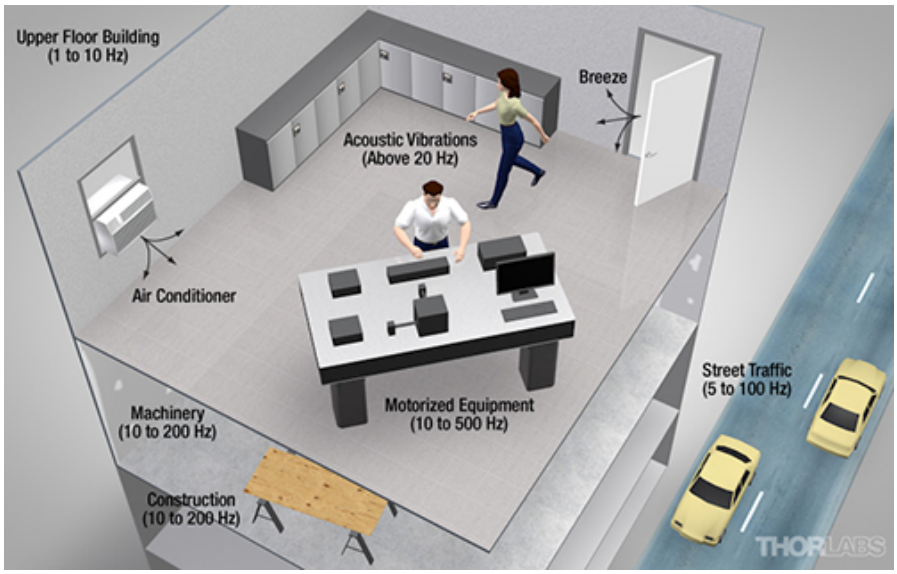

Figure 2.4: Typical vibration sources in a multilevel building. Most disturbances occur in a frequency range from 10 to 200 Hz, which may corrupt the precision measurement performance [40].

2.2 System approaches for precision inline measurements

In order to compensate the disturbing relative motion between the MT and the sample surface to be inspected, a constant alignment throughout the measurement needs to be ensured. Since the idea of inline metrology is to directly integrate the measurement tool after the production process, only limited space is available for the measuring equipment.

Passive concepts (e.g., springs or air bearings) for vibration isolation from external disturbances, which are mainly used in laboratories, suffer from being barely integrable on the small scale [42]. Furthermore, linear passive vibration isolation systems, as shown in Figure 2.5, can be described as damped mass-spring system, with the undamped natural frequency $\omega_0 = \sqrt{k/m}$, where k notates the spring constant and m the mass.
Typical passive vibration isolators have resonance frequencies in the range of 0.5 Hz to several Hz [42]. Due to the second order low-pass characteristics of these systems, a damping below the resonance frequency is not given [43]. In addition, a reduction of the isolator dimension always comes with a decrease of the system mass. This leads to a further increase of the first resonance frequency if the spring

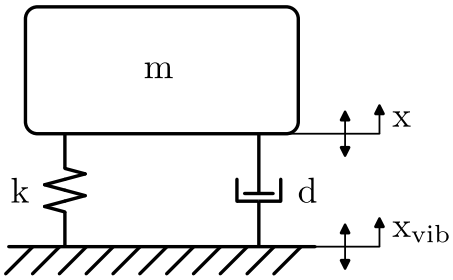

Figure 2.5: Passive vibration isolation concept. The stiffness k and damping d of the vibration isolator to decouple the mass m from external disturbances x_{vib} are selected such that the resulting resonance frequency is as low as possible [21].

constant does not get raised, which further disadvantages the suppression of low frequent vibrations. As a result, measurement tools need to fulfil, besides the high precision measurement itself, additional tasks like vibration compensation in form of active sample tracking. In the last years, several active sample tracking measurement systems have been proposed, mainly working on the Lorentz force actuation principle, which is discussed in the following.

2.2.1 Quasi-zero stiffness actuation

Before discussing state-of-the-art active sample tracking approaches, this section introduces the principle of quasi-zero stiffness actuation in the form of Lorentz actuators, which can enable a mechanical decoupling of the floating mover from the stationary part of the actuator, due to low mechanical stiffness between these parts [21]. Therefore, this actuation principle is used to reduce the transmissibility of disturbances to the measurement tool. Lorentz actuators are working on the Lorentz force principle

$$\boldsymbol{F} = q\left(\boldsymbol{E} + \boldsymbol{v} \times \boldsymbol{B}\right), \tag{2.1}$$

where q is the electric charge, $\boldsymbol{E}$ the electric field, $\boldsymbol{v}$ the velocity of the charge and $\boldsymbol{B}$ the magnetic field density. The electrostatic term $q\boldsymbol{E}$ can be neglected for electromagnetic actuators [21]. The force on a wire with the winding length l_w of a coil being inserted and carrying a current $\boldsymbol{I}$ in the magnetic field B is

$$\boldsymbol{F} = l_w \boldsymbol{I} \times \boldsymbol{B}. \tag{2.2}$$

In Figure 2.6, the Lorentz force principle is schematically illustrated, with a circular coil with N windings and a winding length l_w of the coil being placed in the homogenous part of a magnetic field with the strength B. The resulting force on the current-carrying coil is

$$F = BiNl_w sin\,\alpha, \tag{2.3}$$

where α notates the relative orientation of the current i to the direction of the magnetic field B. It is intended to maximize the force in most cases. Therefore, the term $sin\,\alpha$ is tried to be kept to one by arranging the coil perpendicular to the magnetic field. The ratio $k_m = \frac{F}{i} = const.$ gives a linear constant, which is often called the motor constant of the actuator. As can be seen from Equation 2.3, the force is only depending on the current, the magnetic flux density, and the total wire length of the coil in the magnetic field, but not on the position of the mover, which is why the actuator has almost zero stiffness. This relation holds as long as the wire length l_w in the homogenous field B remains constant [21, 44, 45].

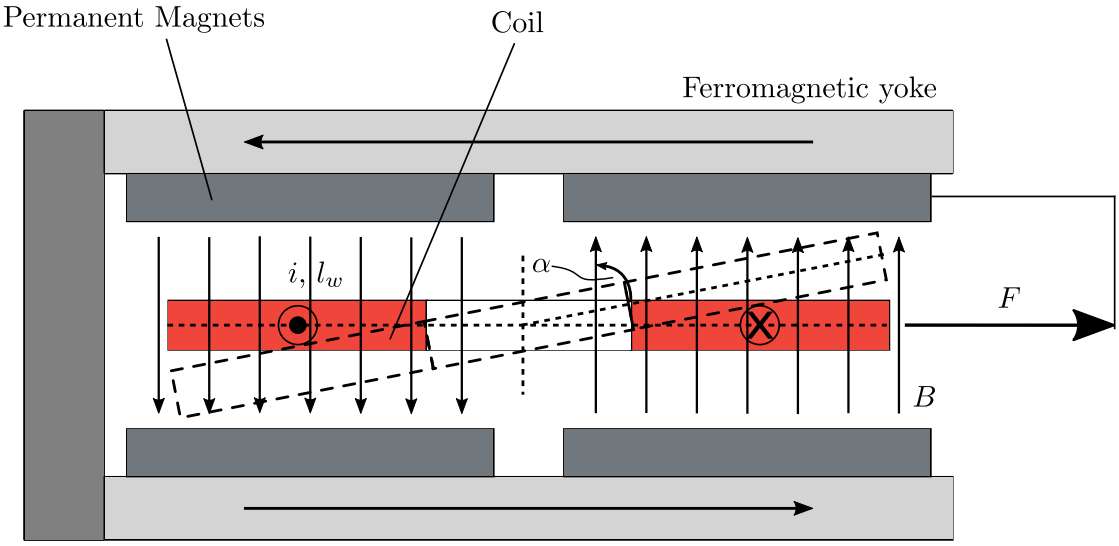

Figure 2.6: Illustration of the working principle of a Lorentz actuator. A coil carrying the current i with the wire length l_w (mover) is placed within the homogeneous part of a magnetic field with the density B, resulting from permanent magnets (PMs) (stator). Depending on the current direction, a bipolar force can be generated based on the Lorentz force principle. The force is maximized by arranging the coil perpendicular to the magnetic field [21].

2.2.2 Vibration isolation concepts

In order to isolate a certain MT or sample from environmental vibrations, the actuators on the previously discussed Lorentz force principle can be used. Recently, a 6 DoF magnetic levitation (MAGLEV) measurement platform, which is capable of actively suppressing vibrations by means of quasi-zero stiffness actuation has been developed [46]. A magnetic table consisting of a 2-D Halbach array of PMs is used as the stator, while the mover consists of a set of coils for generating the horizontal and vertical forces, and Hall sensors are used to measure the mover

position of the carrier relative to the stator, as shown in Figure 2.7. The mover has a size of 50 x 50 mm, has a mass of 53 g and is designed to be equipped with different tools, such as the integration of an atomic force microscope (AFM) for inspection tasks. The travel range of the system is solely limited by the dimensions of the magnetic table. Motions of 1 m/s with maximum accelerations of 10 m/s^2 in the horizontal directions can be performed while achieving positioning resolutions down to 500 nm rms. The field of application of positioning platforms is seen in the semiconductor industry to utilize measurement equipment for different inline inspection tasks.

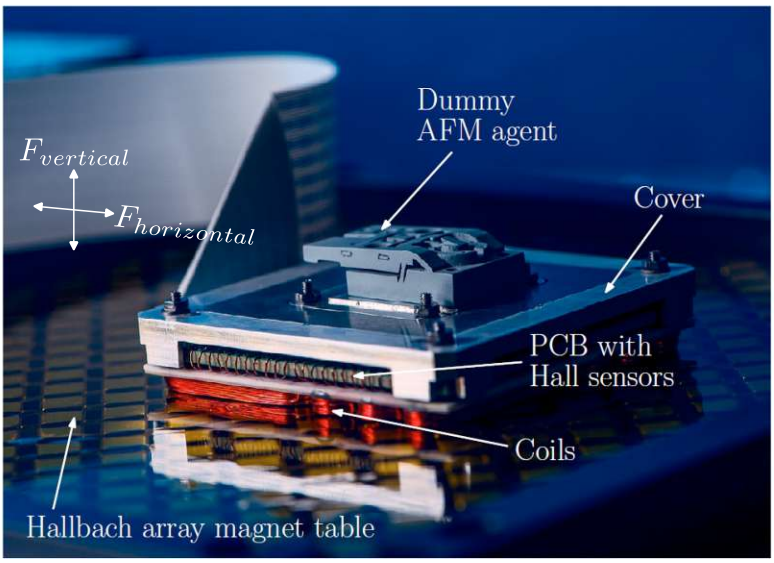

Figure 2.7: Image of a 6 DoF MAGLEV positioning platform working on the principle of quasi-zero stiffness. The mover with an integrated set of coils can be placed at arbitrary locations on the magnetic table realized by 2-D Halbach arrays. The horizontal and vertical forces are generated based on the Lorentz force principle. The use of Hall sensors allow to precisely position the mover along the magnetic table. Different inspection tools, such as an AFM can be mounted on the mover [46].

2.2.3 Vibration compensation by active sample tracking

In contrast to the previously presented vibration isolation concept, vibration compensation can be achieved further by active sample tracking approaches. In [47] a 6 DoF magnetically levitated measurement platform (MP) capable of actively compensating vibrations by using quasi-zero stiffness actuation, as shown in Figure 2.8, is proposed. By means of feedback control, a constant position between the

AFM as a measurement tool on the MP and the sample to be inspected is maintained. In this way, a contactless stiff link between the AFM and the sample is established, actively compensating disturbing relative motion. The gravitational compensation of the MP has been reached by using a permanent magnet array, which, however, limits the operation to horizontal orientation. A set of six coils and PMs are used for positioning the MP precisely relative to the sample surface by measuring the in-plane and out-of-plane sample motion using a combination of capacitive sensors and a heterodyne laser interferometer. A single input single output (SISO) PID control strategy with a closed-loop bandwith (BW) of 35 Hz and 41 Hz for the translational and rotational DoFs, respectively, is used to control each DoF. Residual tracking errors below 50 nm rms have been achieved.

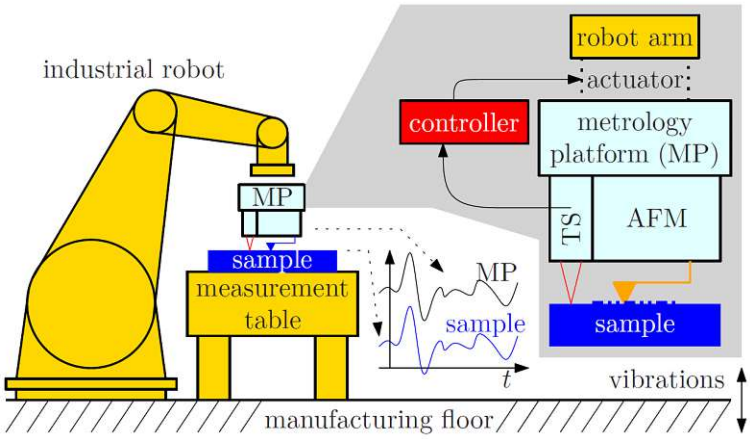

Figure 2.8: A 6 DoF active vibration compensation system implemented on an IR. A stiff link between the MT (AFM) and the sample surface is established by means of feedback control using in-plane and out-of-plane tracking sensors (TSs).

To enable robotic precision 3D measurements in arbitrary orientations, such as required for freeform surfaces, a sample tracking approach purely based on voice coil actuators (VCAs) has been proposed [19]. The author presents a 6 DoF MAGLEV platform, which carries a scanning confocal chromatic sensor as a 3D MT (Figure 2.9). The MP has an actuation range of ±175 µm and ±3 mrad for the translational and rotational DoFs, respectively. A SISO PID control strategy with a BW of 400 Hz is used to control each DoF. The total mass of the system is 5.25 kg, whereas the moving mass is about 900g. In this system, the IR is solely used to statically position the sample tracking measurement module at a desired measurement spot, but is lacking to perform measurements on a moving objects. The MP is capable of reducing vibrations according to the VC-A norm [41] with

15.5 µm rms to 236 nm rms, demonstrating its ability to actively suppress vibrations [48].

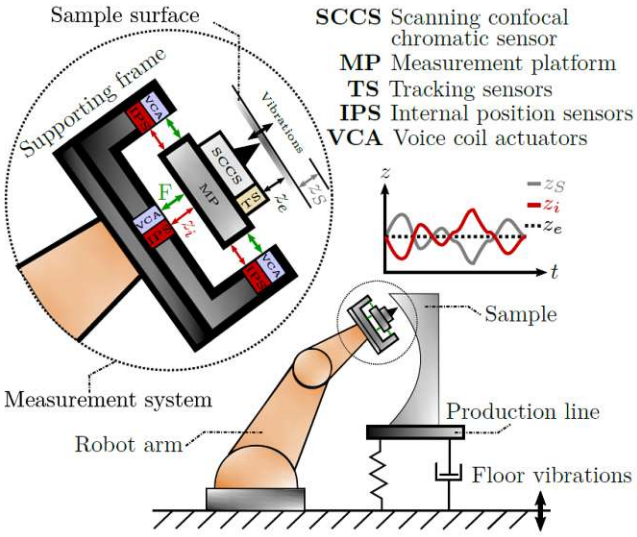

Figure 2.9: System concept of robotic precision 3D measurements on free-form surfaces in vibration-prone environments [19]. A free-floating MP, with an integrated scanning confocal chromatic sensor (SCCS) for 3D measurements on sample surfaces is electromagnetically actuated in all 6 DoFs. By means of feedback control a stiff link between the MT and the sample surface is established using out-of-plane TSs.

2.3 Long-range precision positioning systems

Considering the targeted application of robotic inline 3D measurements on moving objects and the goals defined in Section 1.2, a long-range positioning system is required, which is capable to keep the fine actuated MP within its actuation range. In this relation, dual stage-actuated systems are frequently used.

2.3.1 Dual stage actuation

Requirements, such as high precision positioning and long range actuation, can hardly be met by a single actuation principle. Therefore, distributing these requirements between different actuators is a well known approach that is summarized as dual stage actuation in the literature [21]. Typically in a dual stage actuated system, one actuator is used for the long range (coarse) actuation, whereas the task

of the second actuator is the high precision positioning (fine actuation) [24]. For the scope of active vibration attenuation, high frequent disturbances are compensated by the fine actuator, which is typically based on the Lorentz force principle, while the motion of the coarse actuator keeps the fine actuator within its actuation range [49]. In Figure 2.10, the concept of dual stage actuation is illustrated with the Lorentz actuator (fine actuator) mounted on a long-range linear motor (coarse actuator) [21]. By using, e.g., an interferometer as optical distance sensor, the mover position can be precisely measured. If the mover is repositioned, the distance measured by the internal position sensor (IPS) system can be used to reposition the long-range actuator, maintaining the mover within its limited actuation range. Disturbances acting on the housing of the stator are, as explained in Section 2.2.1, not transmitted to the mover, since there is no mechanical connection.

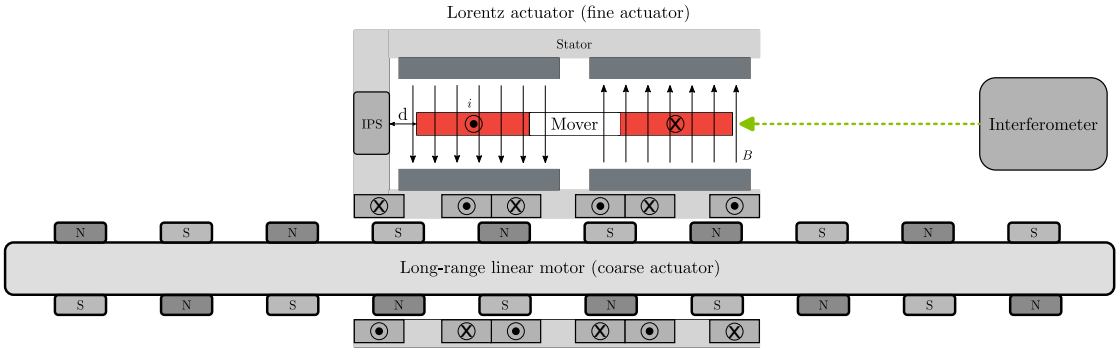

Figure 2.10: Concept of dual stage actuation by combining a fine and long-range actuator. A Lorentz actuator is mounted on a long-range linear motor. An optical sensor, such as an interferometer can be used to track the position of the fine actuator. The coarse actuator needs to be fast enough to maintain the fine actuator within its actuation range. Disturbances acting on the housing of the stator are not transmitted to the mover, since there is no mechanical connection [21].

2.3.2 Motion control

Based on the targeted approach of repositioning an IR to maintain the MP in its actuation range, different motion control strategies are introduced.

2.3.2.1 Feedback control

In a feedback controlled system, a control action is generated by the difference of a desired reference signal r and the feedback, measured by sensors, of the plant $G(s)$ (Figure 2.11). By using feedback control unstable systems can be stabilized. A drawback of the feedback structure is, that the output as well as the sensor

disturbances get amplified, which may be considered in the control design in terms of robustness [21].

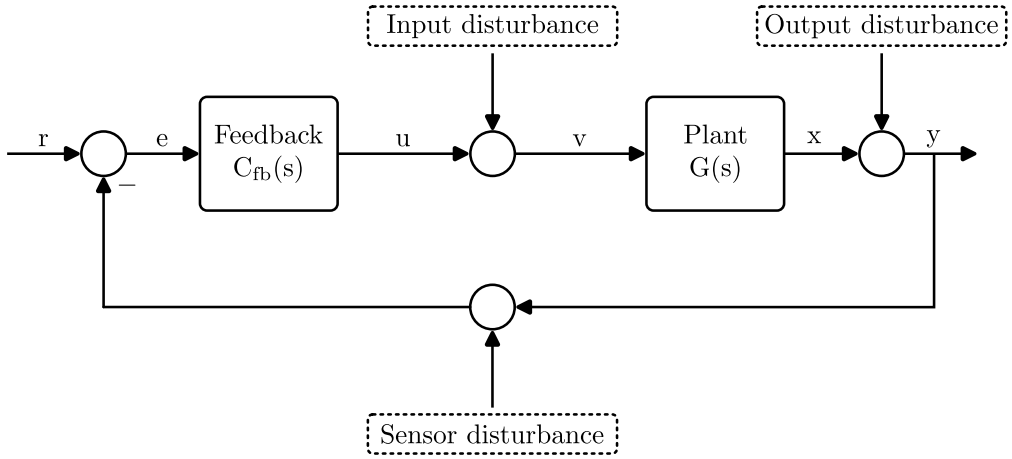

Figure 2.11: SISO feedback control concept. Based on an error e the control action u is calculated. Disturbances occurring at different steps of the feedback control may impact the performance of the system [21].

PID control

Nowadays, up to more than 90 % of all control problems are solved by the application of a PID controller [50–53]. The reason for its incredibly success is the simple design principle, which requires the selection of solely three parameters [54]. The standard form in the continuous time domain of the PID control is

$$u(t) = u_p(t) + u_i(t) + u_d(t) = k_p \left(e(t) + \frac{1}{T_i} \int_0^t e(\tau) d\tau + T_d \frac{de(t)}{dt} \right) \tag{2.4}$$

$$u_p = k_p e(t) \tag{2.5}$$

$$u_i = \frac{k_p}{T_i} \int_0^t e(\tau) d\tau \tag{2.6}$$

$$u_d = k_p T_d \frac{de(t)}{dt}, \tag{2.7}$$

where k_p is the proportional gain, $k_i = \frac{k_p}{T_i}$ the integrator gain and $k_d = k_p T_d$ the differentiator gain. T_i and T_d are the integrator and derivative time constants, respectively. The corresponding discrete version is

$$u(k) = k_p \left(e(k) + \frac{T_s}{T_i} \sum e(k) + \frac{T_d}{T_s} e(k) \right), \tag{2.8}$$

where T_s is the sampling time [54, 55]. For many applications, the differentiator term can be neglected and a PI control is often sufficient for several control

tasks [50]. Within the last centuries, many design rules have been established to derive the control parameters in order to meet different requirements, such as rise time or overshoot. One of the most prominent rules has been developed by Ziegler-Nichols, which allows to design the control based on the step response or frequency response of the system [56]. Although this design principle allows to set the control parameters without much insight of the system, the robustness of such controllers is relatively poor [57]. A systematic way to design a PID controller is to investigate the frequency response of the system in more detail. This allows to systematically design robust and high performant controllers [21]. The design guideline described in [21] allows to implement robust and good performing PID controls for low-stiffness mechatronics positioning systems. Due to the excessive usage of PID controllers in the industry, the performance and functionality have been continuously improved, such as the introduction of anti-wind up strategies, which avoids a limitless integration, when a control variable is saturating by freezing the integrator [53].

LQR control

Beside the application of PID controls, the concept of linear quadratic regulator (LQR) is well established in the scope of precision mechatronics [58, 59]. The LQR represents an optimal state controller, which can be defined for the continuous as well as for the discrete time domain for a set of linear differential equations. In the following, the solution of the LQR is discussed for the fully controllable time-invariant state-space system

$$\dot{\mathbf{x}} = \mathbf{A}\mathbf{x} + \mathbf{B}\mathbf{u} \qquad \mathbf{x}(0) = \mathbf{x}_0 \tag{2.9}$$

$$\mathbf{y} = \mathbf{C}\mathbf{x} + \mathbf{D}\mathbf{u} \tag{2.10}$$

in the continuous time domain. The quadratic cost function with the positive semi-definite matrix $\mathbf{Q}$ and the positive definite matrix $\mathbf{R}$ is defined as follows

$$\mathrm{J} = \int_0^\infty \left(\mathbf{x}^T\mathbf{Q}\mathbf{x} + \mathbf{u}^T\mathbf{R}\mathbf{u}\right) dt, \tag{2.11}$$

which needs to be minimized by

$$\min_{\mathbf{u}} \mathrm{J}. \tag{2.12}$$

Solving the Riccati equation

$$\mathbf{0} = \mathbf{A}^T\mathbf{P} + \mathbf{P}\mathbf{A} - \mathbf{P}\mathbf{B}\mathbf{R}^{-1}\mathbf{B}^T\mathbf{P} \tag{2.13}$$

leads to the optimal state control

$$\mathbf{u}^* = -\mathbf{K}^*\mathbf{x} \tag{2.14}$$
$$\mathbf{K}^* = \mathbf{R}^{-1}\mathbf{B}^T\mathbf{P} \tag{2.15}$$
$$\tag{2.16}$$

with the optimal gain matrix $\mathbf{K}^*$ and control variable $\mathbf{u}^*$ [60].

2.3.2.2 Feedforward control

In many cases, it is desired that a motion x follows a reference signal r, as it is for example common for industrial robots used in the production line to move along predefined trajectories [61]. In order to design a feedforward control, the dynamics of the system has to be well known. The pre-filter $C_{ff}(s)$ is designed, such that it inverts the dynamics of the plant $G(s)$, which enables perfectly control of the motion x without any difference to the reference signal r (Figure 2.12) [21]. Furthermore, a feedforward control can also be designed for such cases, where no dynamics are involved [21], as it is usual for tracking samples on a conveyor system. Since it is common that the velocity trajectory of conveyor systems used in production lines is well known, this information can be used as *a priori* knowledge in the feedforward control [62]. In this case, the pre-filter represents for such cases a simple gain factor [21]. Feedforward control requires no sensors in the system, which is seen advantageous compared to feedback control, since sensor noise cannot be fed back and therefore disturbances are not amplified by the control. Furthermore, no instabilities can be introduced into the system by using feedforward control, which, however, also implies that unstable systems, cannot be stabilized by this control strategy [21].

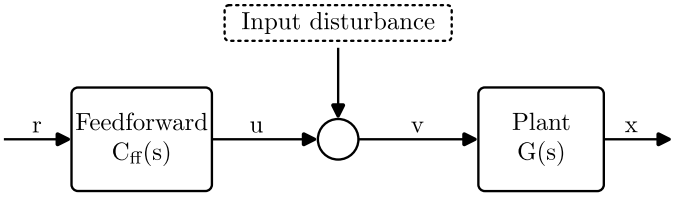

Figure 2.12: SISO feedforward concept. The output signal x follows the by the pre-filter $C_{ff}(s)$ shaped reference signal r [21].

2.3.2.3 Dual stage control

Based on the findings of Section 2.3.1, a dual stage control principle is introduced, for the combination of a long-range (coarse) and precision (fine) actuator. Since

the target of the coarse actuator is to keep the fine actuator within its actuation range, the task of the fine actuator is to quickly response to external disturbances. Therefore, the control of the actuators can be arranged in a parent-child loop, as illustrated in Figure 2.13, with the fine actuator as the parent and the coarse actuator as the child. In this figure, the fine actuator is responsible to compensate the position error signal (PES) induced by the output disturbance d. Based on the control action of the fine actuator the resulting output signal x_{FA} is used as input for the coarse actuation control loop, where the generated output signal x_{CA} aims to compensate the motion of the fine actuator, keeping it in its actuation range [49].

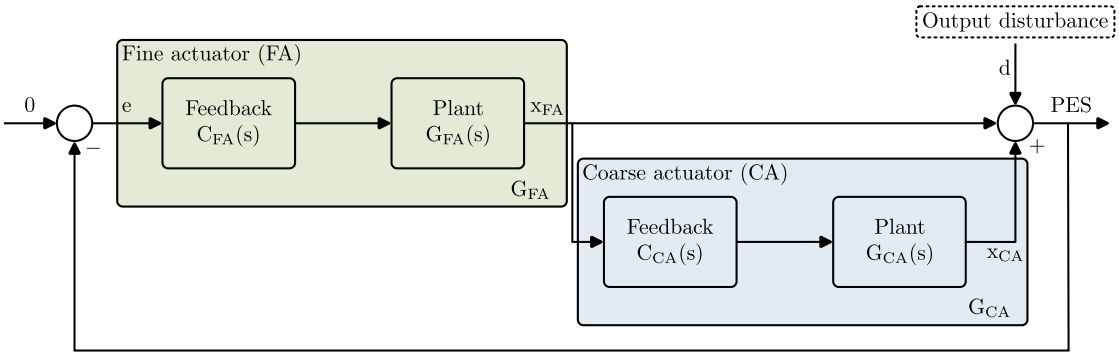

Figure 2.13: Dual stage control concept. Fine and coarse actuator are arranged in a parent-child loop, such that the coarse control is responsible for maintaining the fine actuator in its actuation range. The fine actuator control reacts on high frequent disturbances [49].

2.4 Summary and research questions

Since the limited positioning precision of IRs and external disturbances, such as floor vibrations, both cause relative motion between the MT and sample in the range of several tens of micrometres, active vibration compensation is required to achieve the targeted single- or even sub-micrometer precision in the measurement results. State-of-the-art active sample tracking measurement modules achieve these precisions directly in vibration-prone environments, but are lacking the flexibility to perform measurements on moving objects. Based on the findings of the provided literature review, the combination of IRs and active sample tracking MP shows a huge potential to fill the existing gap related with flexible and versatile alignment of a precision measurement tool enabling the inspection of free-form surfaces directly in challenging industrial environments. This leads to the formulation of the first research question:

Research question 1:
Is it feasible to design a dual stage-controlled robotic system for inline measurement applications with sub-micrometre positioning precision and can the system performance be increased by *a priori* knowledge of the conveyor velocity?

Many production lines use conveyor systems as automatic transportation systems to enable efficient production processes. Though, it is undesirable to stop the conveyor system for reasons of sample inspection, since it would lead to a decrease of production efficiency and throughput. For that reason, a fast and high precision control of the robot position is required to keep the MP in its actuation range, while tracking a sample on a conveyor system and performing precision 3D measurements of the sample surface at the same time. As automatic transportation processes are frequently repetitive the design of more advanced control strategies may be suitable to increase the overall system performance. In this relation, the research question is formulated:

Research question 2:
Is it feasible to perform robotic 3D measurements with sub-micrometre precision on a moving object?

CHAPTER 3

System concept and design

In this chapter, the already existing high precision measurement module to perform measurements in a vibration-prone environment is described. Based on the desired goal of performing high precision measurements on a moving sample placed on a conveyor system, the requirements for the components needed are then discussed.

3.1 Robotic precision 3D measurement system

As discussed in Section 2.1.1, active sample tracking approaches are indispensable to enable precision inline measurements, as they can establish the required lab-like conditions for the 3D measurement tool (MT). The disturbing relative motion between the MT and the sample can either be induced by external disturbances, such as environmental vibrations, or by the limited positioning accuracy of an industrial robot (IR).

In order to compensate this corruptive relative motion, the provided precision 3D measurement module [20], presented in Figure 3.1, actively tracks a sample surface in all 6 degree of freedoms (DoFs) and can be operated in arbitrary operation orientations. The measurement module consists of three main parts: the supporting frame, the measurement platform (MP) and the scanning confocal chromatic sensor (SCCS). The MP is electromagnetically levitated and actuated by using eight identical voice coil actuators (VCAs), each capable of providing a force of 20 N continuously. The housing of the permanent magnets are mounted on the supporting frame and the coils are fixed at the MP. With the MP being

in its centre position it provides an actuation range of ±175 µm and ±3 mrad in the translational and rotational DoFs, respectively. The motion of the MP relative to the supporting frame is measured by an internal position sensor (IPS) system, which is a set of six capacitive displacement sensors. To measure the MP's out-of-plane position relative to a sample surface, three tracking sensors (TSs), TS1 ... TS3, which are also capacitive displacement sensors, are mounted on the MP. The in-plane position of the sample is measured by two position sensitive detectors (PSDs) (TS45 and TS67), placed at the corners of the MP, in combination with two laser diodes as markers [63]. The SCCS [64] is embedded in the MP and capable of performing precision 3D images. By manipulating the optical path of a high precision 1D confocal chromatic sensor (CCS) with a 2D fast steering mirror (FSM), a measurement volume of $0.35 \times 0.25 \times 1.8\,\mathrm{mm}^3$ is achieved with a lateral and axial resolution of 2.5 µm and 2.5 nm, respectively. The mass of the entire measurement module is 5.25 kg, whereby the MP, which needs to be electromagnetically levitated and actuated, contributes about 900 g.

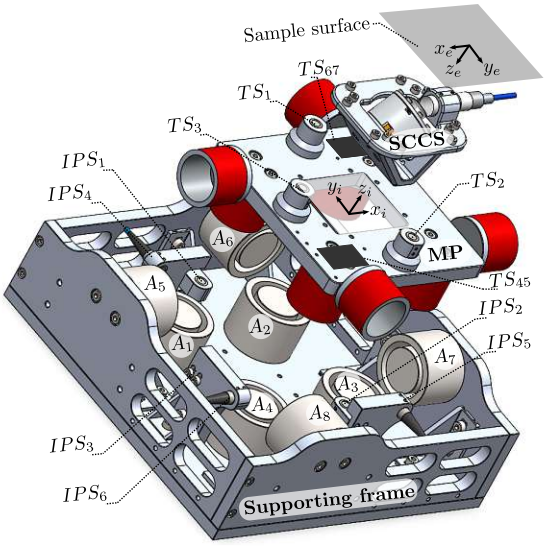

Figure 3.1: Exploded view of the functional components of the 3D measurement module. A1 ... A8 are the VCAs to actuate the MP in all 6 DoFs. IPS1 ... IPS6 and TS1 ... TS67 are the internal position and tracking sensors, respectively. The SCCS is embedded into the MP as 3D MT [20].

Figure 3.2a shows the top view of the measurement module and the corresponding sample box, which is used to provide the required stiff connection between the markers and the sample surface. The sample box in Figure 3.2b includes conductive targets for the three capacitive TSs, the laser diode-based markers for the in-plane TS system and a mounting for the sample surface to be precisely 3D imaged [63].

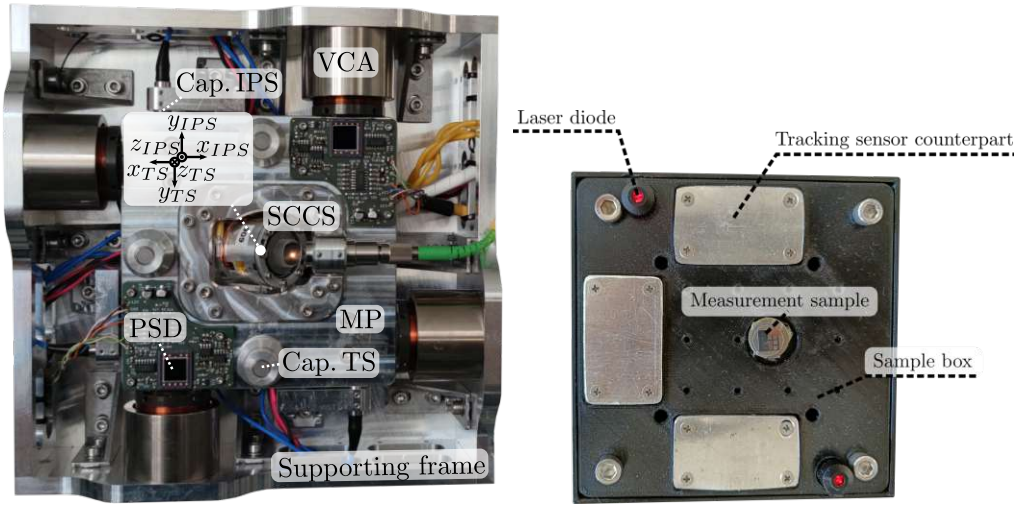

(a) (b)

Figure 3.2: Top view of the measurement module with the corresponding sample box. (a) shows the individual system components of the measurement module. In (b) the corresponding sample box is illustrated, which is equipped with markers and targets for the TSs of the measurement module, and a mounting for a sample that can be 3D imaged by the SCCS [20].

The MP can be operated either in a stabilization or in tracking mode, which can be selected based on a cross-fading error gain (CFEG), as described in [65]. The stabilization mode allows to position the MP relative to the supporting frame, whereas the tracking mode actively compensates the relative motions between the MP and a sample. In tracking mode, the MP establishes a stiff and contactless link between the MP and the sample, generating lab-like conditions in a vibration-prone environment. The control of the MP and the FSM as well as the processing of the sensor data are implemented on a dSPACE MicroLabBox (MicroLabBox, dSPACE GmbH, Paderborn, Germany), which operates at a sampling frequency of 25 kHz. Figure 3.3 presents the 3D measurement module mounted to a robot arm, which is discussed in detail in Chapter 4. Up to this point, the robot is solely controlled via the control panel, i.e. the measurement module is positioned manually relative to a sample. With an eye towards the targeted application (see Section 1.2), the actuation range of the MP is limited to 125 µm and 1.5 mrad for the translational and rotational DoFs, respectively, by a software-implemented safety feature to prevent mechanical damage of the measurement module and its components.

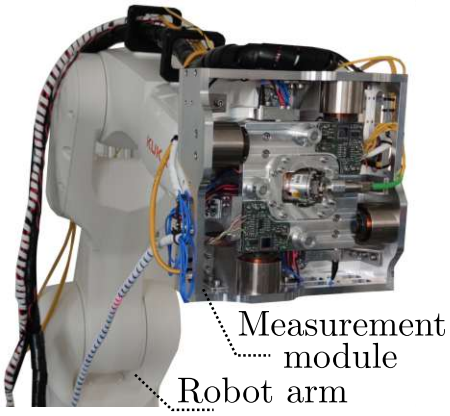

Figure 3.3: Precision 3D measurement integrated as an endeffector to an IR.

3.2 Dual stage-controlled robotic measurement system design

Based on the findings of the literature review and the research questions defined in Chapter 2, the targeted system concept of robotic precision 3D measurement on moving objects is schematically illustrated in Figure 3.4a. For reasons of clarity, the system concept is presented exemplarily for one DoF. The sample mounted on the sample box (see Section 3.1) is placed on a conveyor system. With the MP in tracking mode, disturbance-induced, higher frequent relative motion between the MP and the sample surface is compensated, i.e. $x_{TS} = const.$. A by the conveyor velocity $v_{conveyor}$ induced relative motion $x_{conveyor}$ smaller than the MP's translational actuation range of about $\pm 175\,\mu m$ can be measured with the IPS signal x_{IPS}. Based on the error between the actual measured internal MP position x_{IPS} and its centre position $x_{IPS,ref}$, the IR position controller repositions the IR's TCP. In this way, the MP is maintained in its centre position, enabling a dual stage-controlled repositioning of the IR, with the MP's sample tracking control being the fast and precise inner control loop. As the moving sample is actively tracked by the MP, the targeted stiff link between the SCCS as 3D MT and the sample is established, compensating for both the conveyor- and disturbance-induced relative motion.
Considering the provided sample tracking 3D measurement system presented in Section 3.1 and the concept of robotic precision 3D measurements on moving objects in Figure 3.4a, the requirements on the communication interface between the measurement module and the IR control unit as well as on the conveyor system are discussed in the following.

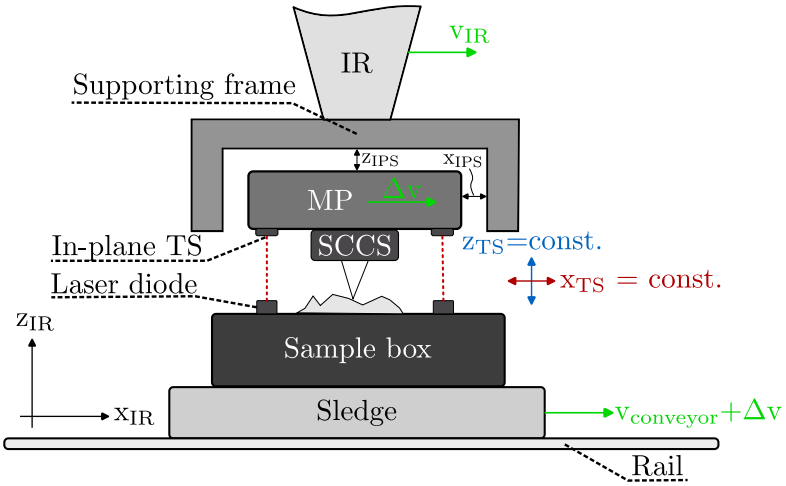

(a) Dual stage-actuated system for precise 3D measurements on moving objects.

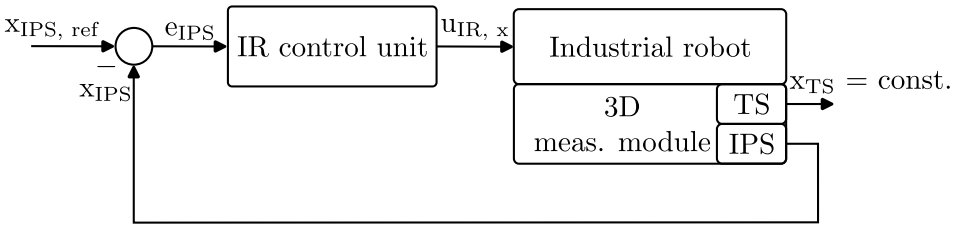

(b) According dual stage control concept.

Figure 3.4: System concept for precision robotic inline 3D measurements on moving objects. (a) The MP is in tracking mode, maintaining a constant position $x_{TS} = const.$ between the MT on the MP relative to the sample on the sample box. The by the conveyor velocity $v_{conveyor}$ induced relative motion $x_{conveyor}$ is measured with the IPS signal x_{IPS}. (b) Based on the error between the MP's internal centre $x_{IPS,ref}$ and measured position x_{IPS}, the IR's position control precisely repositions the IR's TCP, resulting in a motion with the velocity v_{IR}. Disturbance-induced relative motion between the sample and the MT by the velocity Δv are compensated by the active sample tracking MP. During the tracking of the moving sample, the SCCS can perform precision 3D images.

Real-time robot control communication interface

In order to enable the desired robust and precise repositioning of the IR, a real-time capable interface between the rapid-prototyping system, which is used for signal

processing and control of the sample tracking 3D measurement module, and the IR control unit is required. As the internal MP position x_{IPS} is relative, an IR repositioning based on relative correction values is favourable. With consideration of the targeted sample motion speed of up to 10 mm/s and half of the translational MP actuation range of ±175 µm, a minimum IR control cycle time of 17.5 ms can be derived.

Conveyor system

The conveyor system illustrated in Figure 3.4a represents an industrial production line and is used to put the sample mounted on the sample box in motion. In a first step towards the targeted concept of precise robotic 3D measurements on moving object, sample speeds of up to 10 mm/s are considered, which serves a first design guideline for the conveyor system to be implemented in Chapter 4. Moreover, the velocity should be continuously controllable between standstill and the maximum conveyor speed. As the conveyor velocity is typically known in industrial applications and may be used as *a priori* knowledge for the subsequent IR repositioning control, the conveyor system velocity should be applicable to the IR control unit.

CHAPTER 4

System implementation

Based on the design guideline derived in Chapter 3, the dual stage-controlled robotic system for inline 3D measurements on moving objects is step by step systematically implemented. Figure 4.1 provides an overview of the fully implemented system, with the individual system components discussed in the following.

4.1 Industrial robot

For the targeted application of high precision robotic inline measurements on moving objects, a 6 degree of freedom (DoF) industrial robot KUKA KR 10 R900-2 (KUKA AG, Augsburg Germany), as shown in Figure 4.2, is selected. The industrial robot can operate in a physical working volume of 2.84 m^3 and achieves a position repeatability of $\pm 20\,\mu m$. The workspace configuration is shown in Figure 4.3. The flange of the robot is able to hold a nominal load of 6 kg, which is sufficient for carrying the 3D measurement module. The control unit KUKA KR C4 compact (KUKA AG, Augsburg Germany) in combination with the development environment KUKA WorkVisual allows to adjust several configurations such as the configuration of different communication interfaces (e.g., PROFINET, PROFIBUS, EtherCAT, ...). Furthermore, digital and analog I/Os of the control unit can be configured and connected.

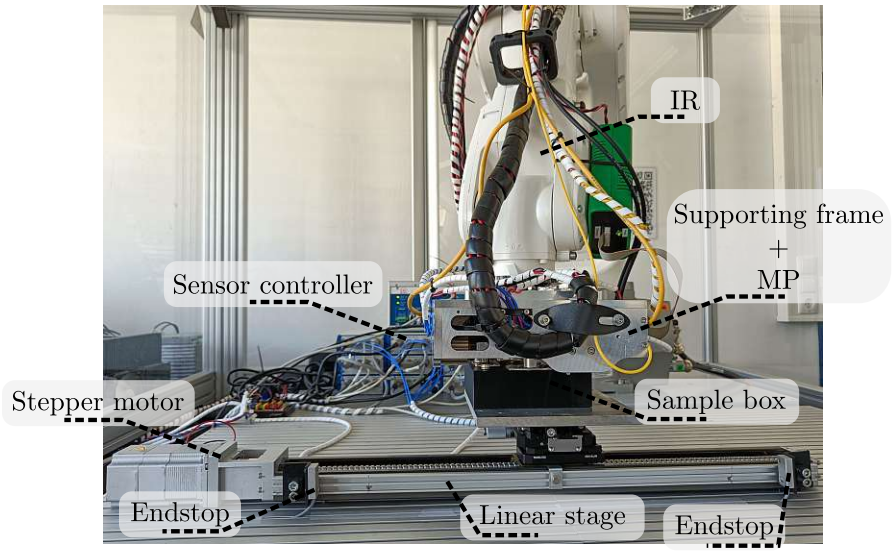

Figure 4.1: Overview of the system components integrated in the dual stage-controlled robotic system for inline 3D measurements on moving objects. The measurement module mounted to the industrial robot (IR) is placed above the sample box, such that the tracking sensors (TSs) are in range, measuring the relative in- and out-of-plane motion between the measurement tool (MT) and the sample. The sample box is placed on the sledge of a linear stage, which is actuated by a stepper motor. Endstops are mounted at both ends of the conveyor system.

4.2 Rapid prototyping system and communication interface

With consideration of the requirement to control the robot repositioning in real-time, this section introduces the used rapid prototyping solution and communication interfaces in this thesis. In Figure 4.4, an overview of the communication structure is presented.

4.2.1 Robot Sensor Interface (RSI)

The KUKA RSI is an optional package to extend the functionality of the robot, which allows data exchange between the robot control and external systems, such as sensors and PLCs, in real-time. Furthermore, the signal of the external system can be processed within the RSI to manipulate the motion of the robot. For that reason, it operates with a predefined cycle time of 4 ms (#IPO_FAST, default) or 12 ms (#IPO).

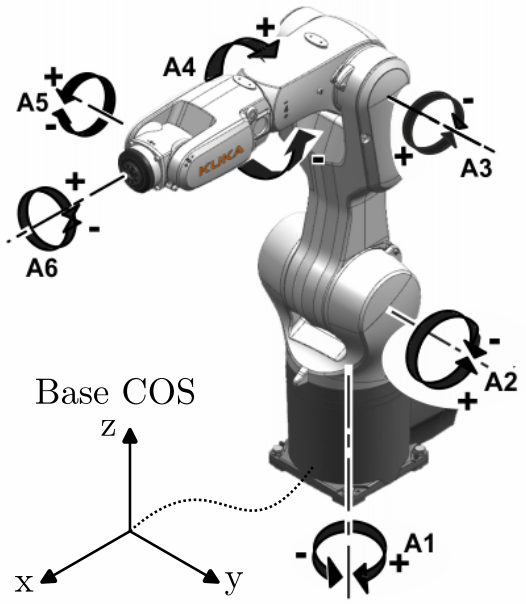

Figure 4.2: Industrial robot KUKA KR 10 R900-2 with the corresponding joint rotation directions [66].

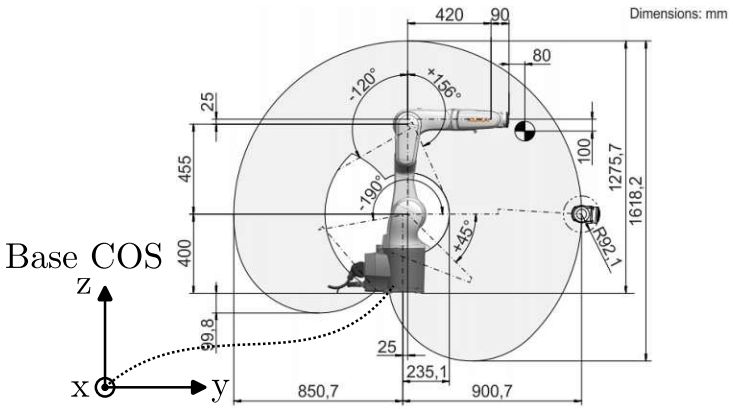

Figure 4.3: Corresponding workspace of the KUKA KR 10 R900-2 [66].

Therefore, real-time capable field-buses, e.g., EtherCAT, can be used [67]. An additional field-bus coupler (EtherCAT-Bridge EL6695-1001) is implemented to establish a communication between the robot control unit (KUKA KR C4) and an externally PLC [68]. Figure 4.5 shows the integration of an external field-bus in the RSI. The RSI provides 8192 bits for the in- and output side. Within WorkVisual, which is the user interface of the robot control unit, it is possible to group the bits in the I/O connection tab. This further allows to define other data-types,

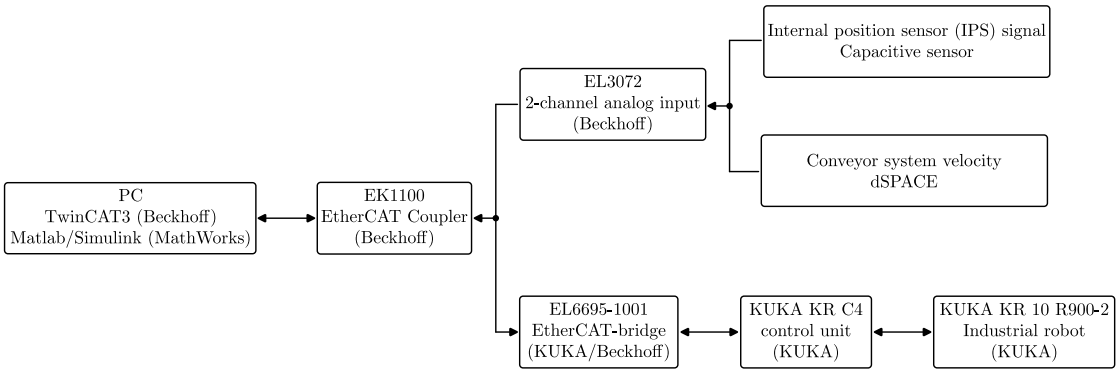

Figure 4.4: Overview of the real-time communication structure. The internal position sensor (IPS) signal and the conveyor velocity is acquired by the Beckhoff DAQ system components. Based on the provided data, which gets further processed in the rapid prototyping solution TwinCAT 3, the IR's tool center point (TCP) is repositioned accordingly. The Robot Sensor Interface (RSI) is used to establish a real-time communication between the IR control unit and the Beckhoff programmable logic control (PLC).

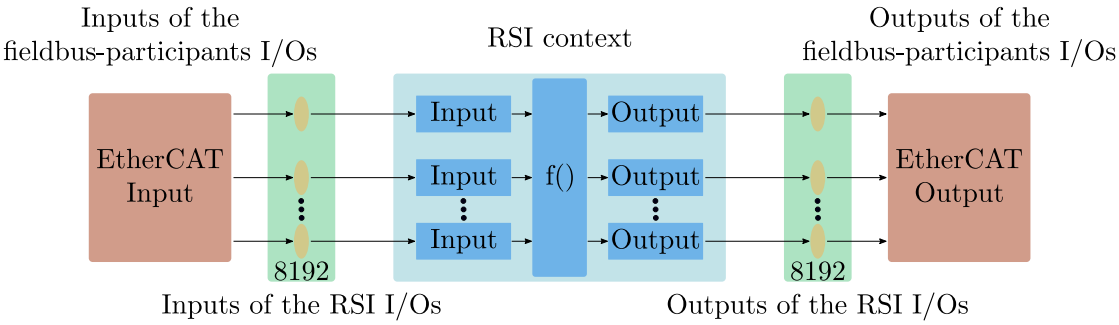

Figure 4.5: Communication principle of the RSI. The 8192 in- and output bits can be grouped to define different datatypes which can be then connected to the I/Os of the RSI context. The block f() allows to create user-defined programs in a function block diagram like user interface. These programs allow to implement control strategies to reposition the IR's TCP based on data provided by the RSI inputs. [67].

as for example a BOOL, consisting of 8 Bit or a DWORD taking 32 Bit. Those grouped I/Os can be connected to the in- and outputs of the field-bus participants accordingly. The actual processing of the sensor data is realized by a so called RSI context, created in WorkVisual, and programmed in a graphical editor, similar to the IEC 61131-3 function block diagram [69]. The RSI context provides many different objects, summarized in a library, to program the robot. Table 4.1 lists

the used RSI objects.

Table 4.1: Summary of the used RSI objects [67].

Type	Description
Communication objects	
DigIn	Definition of digital inputs in the RSI context
DigOut	Definition of digital outputs in the RSI context
Monitor	Allows to visualize up to 24 RSI signals
RSI-objects for motion correction	
PosCorr	Cartesian motion correction with limitation
Stop	Stops the motion by a rising edge
RSI-objects for motion monitoring	
PosCorrMon	Limitation of the total cartesian correction
RSI-objects to read robot related data	
PosAct	Provides the current cartesian robot position

The created RSI context can be loaded in a separate KRL (KUKA Robot Language) program. Therefore, a RSI container needs to be assigned with the command *RSI_CREATE()*, which loads the stated RSI context. The command *RSI_ON()* starts the RSI context, in either absolute (default) or relative motion correction. From this point on the robot motion is controlled by the transmitted correction values from the external system. Based on the received correction values an internal control loop is planning the robot motion trajectory, which cannot be modified by the user. Figure 4.6 illustrates the difference between both modes.
Starting from a point P0, a new position in absolute correction mode is reached by calculating the new position from its origin (Figure 4.6a). In comparison, the new position in relative correction mode (Figure 4.6b) is reached by calculating the distance between the new and the actual position and sending this correction value to the robot control. Hence, the overall motion of the robot is a cumulative sum of the partial corrections.

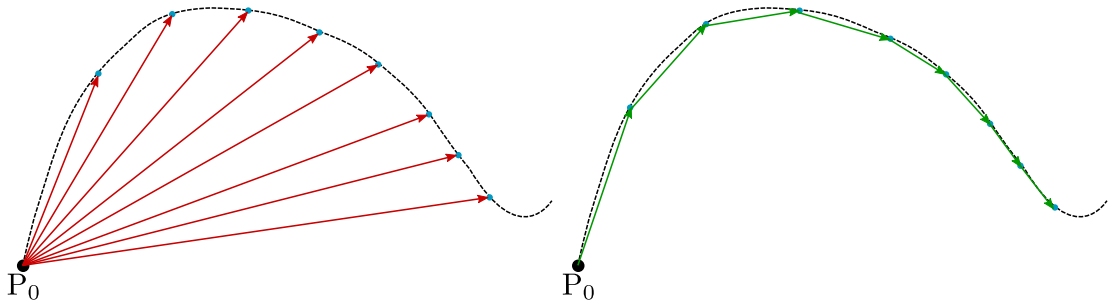

(a) absolute correction (b) relative correction

Figure 4.6: Absolute and relative sensor-based motion correction provided by the RSI. In (a), the IR is repositioned in absolute correction values. A new point is reached by calculating the distance to a starting point P0. A relative repositioning of the IR is illustrated in (b). A new point is reached by calculating the relative distance to the actual position [67].

Within this approach, the RSI is configured in relative correction mode with a cycle time of 4 ms. In the RSI context, the command *PosCorr* is used for a cartesian correction of the TCP. The reason for this configuration is that the measurement platform (MP) compensates relative motion with respect to the sample. The disturbance compensating MP motion is measured by the IPSs, which can then be directly used to reposition the TCP of the robot, maintaining the MP in its centre position.

4.2.2 Rapid prototyping system

As described in the previous section the robot motion can be influenced in real-time via using the RSI. Considering the system concept in Fig 3.4a, the IPS provided by the MP being in tracking mode needs to be processed in order to precisely reposition the IR to maintain the MP in its centre position. For that reason, the industrial DAQ (data acquisition) system (EK1100, EL3702, EL6695-1001, Beckhoff Automation GmbH & Co.KG, Verl, Germany) is used, as show in Figure 4.4. The software solution TwinCAT3 (Beckhoff Automation GmbH & Co.KG, Verl, Germany) allows to process the data provided via the EK1100 EtherCAT coupler and can be operated on personal computers. Furthermore, the TE1400 TwinCAT3 Target for Simulink®(Beckhoff Automation GmbH & Co.KG, Verl, Germany) can be optionally installed on TwinCAT3. This software package allows to use projects created with Simulink (The MathWorks, Inc., Natick, Massachusetts, USA) in TwinCAT3 by translating the entire project into C/C++ code. In TwinCAT3, the integrated Simulink project is deployed on an isolated processor core with the further possibility to define a specific cycle time, allowing to generate real-time

capable solutions. As shown in Figure 4.7, a Simulink project responsible for the communication and the signal processing is generated. A cycle time of 80 µs is assigned to this project. The aim of this task is to handle the communication with the 3D measurement module related components. Furthermore, the IPS errors are calculated based on the reference centre positions of the MP in every cycle. A second Simulink project is deployed and running on the same core, but with a cycle time of 4 ms, equally to the cycle time of the RSI as discussed in Section 4.2.1. The task of this program is to generate the motion correction values for the IR based on the received IPS error signals. The calculated correction values are then internally send back to the communication and signal preprocessing task, where those values are transmitted to the EtherCAT-bridge.

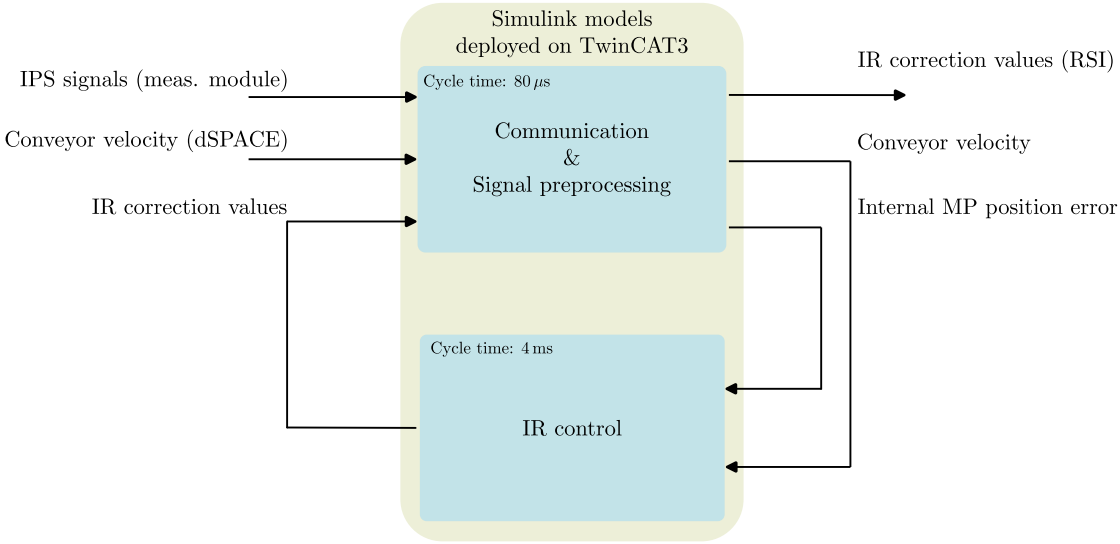

Figure 4.7: Overview of the implemented Simulink models on TwinCAT 3. A communication & signal processing project is deployed on an isolated processor core of the engineering PC and runs with a cycle time of 80 µs. This project is responsible for calculating the internal MP position error signal based on the IPS signals and centre reference positions of the MP, and handles the communication with 3D measurement module related components. The IR control project is deployed on the same core and runs with a cycle time of 4 ms, equally to the cycle time of the RSI. Based on the received internal MP position error signals and conveyor velocity, a correction value to reposition the IR is calculated and applied by the communication & signal processing project to the RSI.

4.3 Sample conveyor system

Based on the requirements of Chapter 3, a linear stage with a two-phase stepper motor and a range of 400 mm is selected. The sledge of the conveyor system provides mounting holes for flexible mounting options. In Figure 4.8 the assembled conveyor system is presented, with the sample box rigidly connected to the conveyor sledge. Since the intended conveyor system has no internal safety measures to detect a

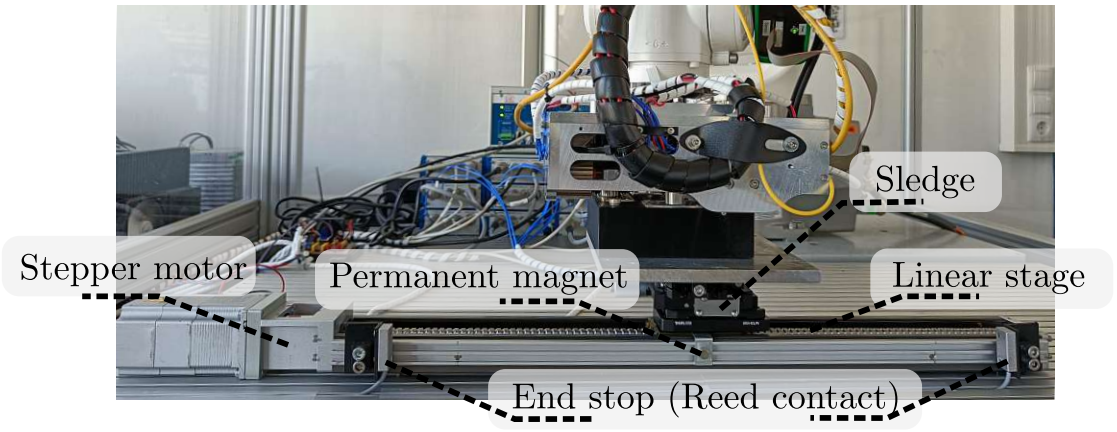

Figure 4.8: Sample conveying system. A linear stage is actuated by a two-phase stepper motor. The conveyor sledge provides mounting holes for flexible mounting options. Two reed contacts are installed at both ends of the stage and a permanent magnet (PM) is mounted on the sledge.

run-up of the conveyor sledge additional end stops, in form of reed switches are mounted at both ends of the stage (Figure 4.8). The purpose of these end stops is to avoid damage to the system components, if the sledge exceeds the maximum travel range of 400 mm. Therefore, the reed switch (RS Pro, RS Components Handelsgesellschaft m.b.H, Gmünd, Austria) are used as presented in Figure 4.9a. A permanent magnet is placed on the sledge, as shown in Figure 4.8, which triggers the switch if the sledge gets too close to the according end stops. Figure 4.9b shows the read-out circuit for detecting a run-up. A constant voltage $U_0 = 5\,\mathrm{V}$ is applied and the resistor $R_1 = 100\,\Omega$ is used to limit the current to 50 mA. At a conveyor run-up, the voltage drop at the reed switch is detected by a digital input of the dSPACE system. Further safety measures are implemented to take action, if a run-up of the sledge is detected. In such a case, the robot, conveyor and MP are stopped immediately, to avoid damage to one of the components.

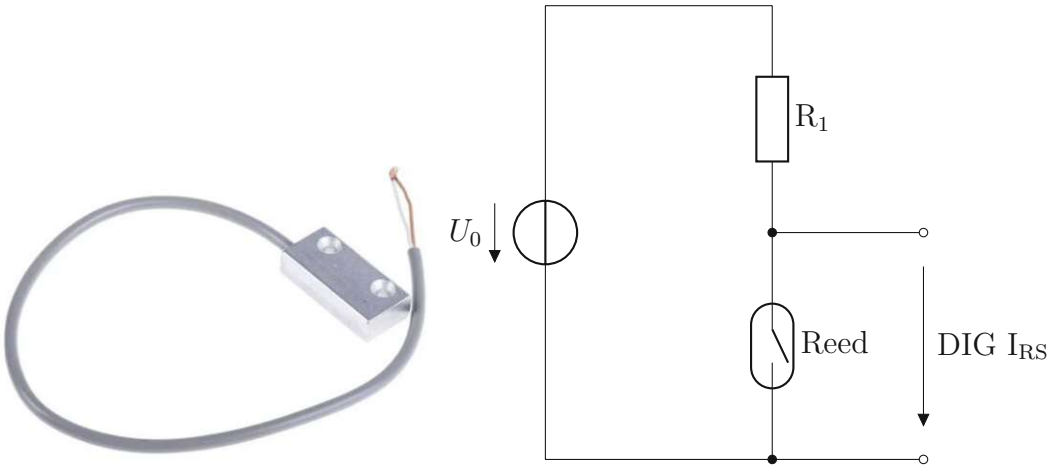

Figure 4.9: Overview of the used reed switch and read-out circuit to detect a run-up. In (a) an illustration of the RS PRO Reed Switch is shown. (b) shows the corresponding read-out circuit to determine if the sledge exceeds the maximum travelling distance on the linear stage.

4.3.1 Velocity control of the conveyor system

Since the velocity of the conveyor system is required to be continuously and precisely controllable, it is decided to actuate a linear stage with a two-phase stepper motor. Therefore, the motor driver TMC2209-V1.2 (BIGTREETECH, Ltd., Shenzhen, China) to control the velocity is used. The motor driver is capable of operating at a continuos current of 2 A and can provide up to 256 micro-steps. Figure 4.10 shows the circuit to control the velocity of the linear stage. In order to control the

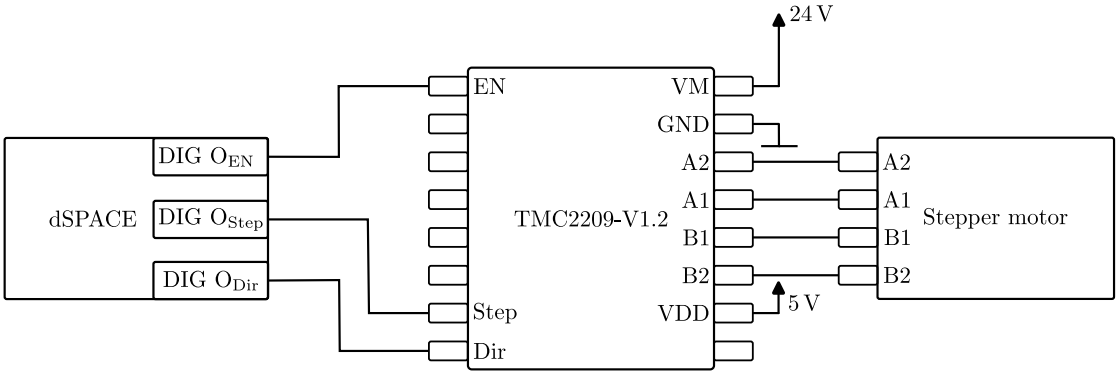

Figure 4.10: Block diagram of the conveyor velocity control.

velocity of the conveyor system and to apply a desired motion trajectory to the

sample (Figure 4.11a), a corresponding rectangular signal with varying frequency as shown in Figure 4.11b needs to be applied to the motor driver. Digital outputs of the rapid prototyping system dSPACE, as described in Section 3.1, are used to interact with the motor driver. The digital output DIG O_{EN} enables/disables the motor driver. By sending pulsed signals, as shown in Figure 4.11b, over the digital output DIG O_{Step} to the input Step of the motor driver the resulting drive of the stepper motor can be adjusted. With the input Dir of the motor driver the rotation direction of the stepper motor can be adjusted. The expected linear relationship between the frequency of the applied rectangular signal and the desired velocity has been verified by experiments. Using the constant $k = 240\,\frac{\text{Hz}}{\text{mm/s}}$, a targeted velocity trajectory is transformed into a frequency output.

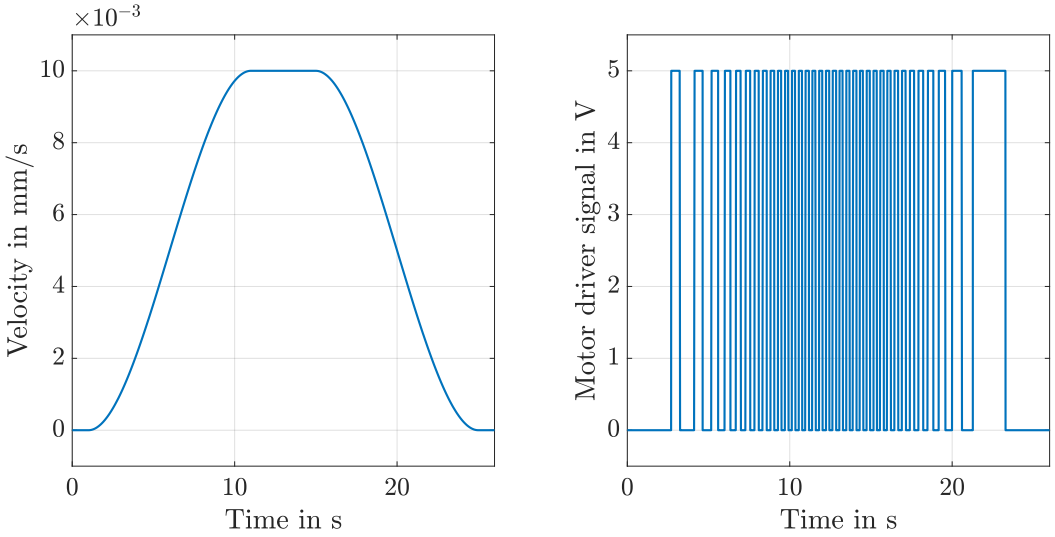

(a) Velocity trajectory.

(b) Frequency modulated rectangular signal.

Figure 4.11: Velocity control of the conveyor system. (a) shows the velocity trajectory with a maximum of 0.01 mm/s. The corresponding frequency modulated rectangular signals to control the conveyor system velocity is shown in (b).

CHAPTER 5

System identification and control design

In this chapter, the dynamics of the robot in all six degree of freedoms (DoFs) are identified. Based on these results, the dual stage control to precisely reposition the industrial robot's tool center point (TCP) to maintain the measurement platform (MP) in its centre position relative to the industrial robot (IR) is designed. With consideration of the system concept presented in Figure 3.4a and the MP operated in tracking mode, a motion induced by the conveyor system leads to a displacement of the MP from its centre position measured by the internal position sensors (IPSs). Using this measured internal MP position error, the aim of the robot control to be designed is to precisely reposition the IR, such that the sample motion can be traced robustly along the entire conveyor range.

5.1 Identification of the industrial robot dynamics

The identification of the IR dynamics allows to systematically design a tailored IR repositioning control with desired properties, such as rise time, overshoot and robustness. In general, the dynamics of IRs are pose depending [70], which is why the exact system dynamics have to be identified with respect to the subsequent control design. This means the characteristics of the system varies at different positions in the workspace. Since it is aimed to track the sample motion over the full range of the conveyor system, the dynamics of the IR are identified at the left and right end as well as in the centre of the conveyor range, determining the variance of the IR dynamics for each DoF (Figure 5.1).

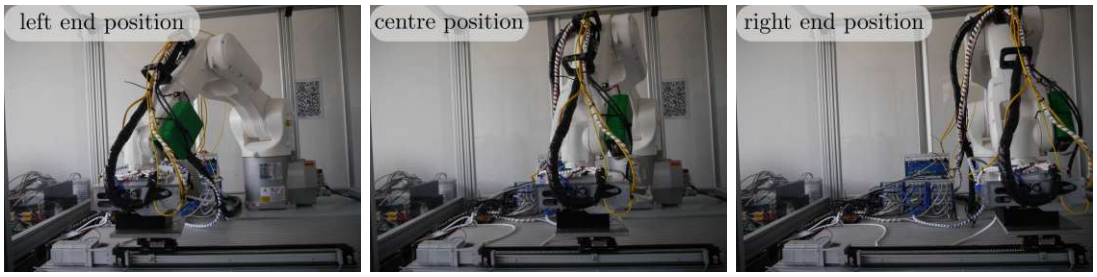

(a) left end position (b) centre position (c) right end position

Figure 5.1: Identification of the IR dynamics in each DoF in different poses along the conveyor travel range.

In each of these poses, the in- and out-of-plane tracking sensors (TSs) of the MP are well placed within their measurement range. Figure 5.2 shows the block diagram of the setup to identify the IR dynamics. Throughout the identification process, the MP actively tracks the sample motion, establishing a stiff link to the sample. Separately for each DoF, a frequency sweep of the harmonic reference signal

$$IR_{ref,i} = Asin(2\pi f), \quad i = x,\ y,\ z,\ \phi_x,\ \phi_y,\ \phi_z \tag{5.1}$$

in the range of 0.1 Hz to 50 Hz is applied to the IR control unit. The amplitude A is set to 10 µm and 0.0873 mrad for the translational and rotational DoFs, respectively. As discussed in Section 4.2.1, the Robot Sensor Interface (RSI) needs

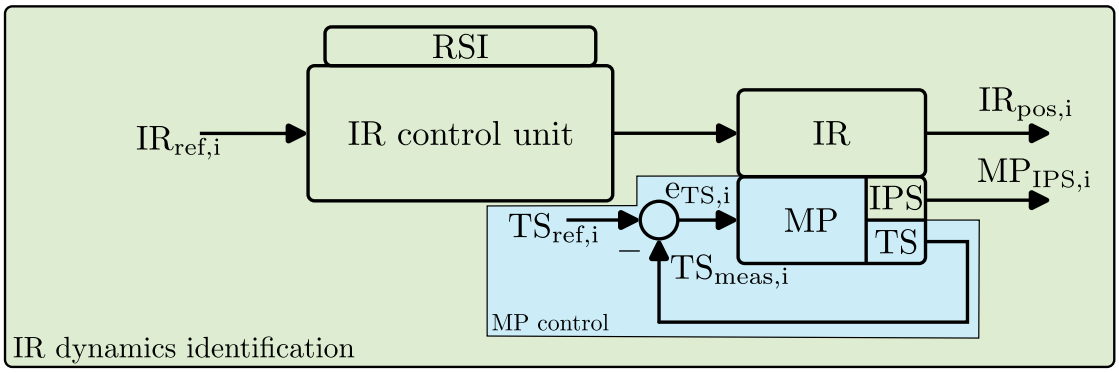

Figure 5.2: Block diagram illustrating the identification of the IR dynamics. The tracking control of the MP is shown in the blue section, which is active throughout the identification process. The reference signal $IR_{ref,i}$ ($i = x,\ y,\ z,\ \phi_x,\ \phi_y,\ \phi_z$) is applied to the IR control unit in each DoF by means of a frequency sweep in the range of 0.1 Hz to 50 Hz. The by the IR performed motion is measured by the IR encoders ($Rob_{pos,i}$) and the IPS signals ($MP_{IPS,i}$).

to be configured in absolute cartesian correction mode for the identification process

in order to achieve the correct IR motion based on the reference signal. The measured dynamics in a certain DoF is given by

$$G_{i,j} = \frac{MP_{IPS,j}}{IR_{ref,i}} \quad i,\, j = x,\, y,\, z,\, \phi_x,\, \phi_y,\, \phi_z \tag{5.2}$$

where the combination of the indices with $i \neq j$ indicates crosstalk. In order to avoid Abbe errors in the measured TCP position, as discussed in Section 2.1.2, the internal MP position MP_{IPS} is used instead of the IR position measured by the IR encoder system. Considering the two coordinate systems (COSs) in the MP and the TCP, the COSs are the same except for a constant offset in z-direction (Figure 5.3). Since the MP is in active sample tracking mode, the excitation of the IR is compensated by an opposed motion of the MP, resulting in a phase shift of 180 °, in the identified dynamics. Figure 5.4 exemplarily illustrates the dynamics of DoF x

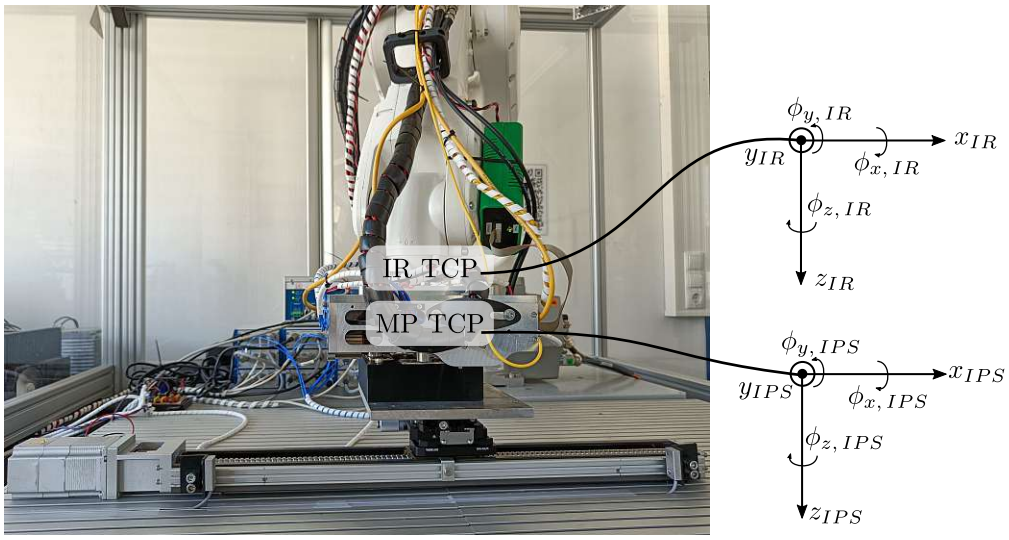

Figure 5.3: Identification of the IR in each DoF placed in the centre of the conveyor travel range. The corresponding coordinate systems for the IR and MP TCP show a constant offset in z-direction.

with the TCP in centre position above the conveyor system, separately identified with the IR encoder and the MP's IPS system. From this comparison, it can be seen that for frequencies below 2 Hz both magnitude and phase are measured similarly, except for the aforementioned 180 ° phase shift, which needs to be considered, when designing the subsequent control to precisely reposition the IR. However, the resonance peak at 26.8 Hz is not detected correctly by the IR encoder, which is most probably Abbe error related.

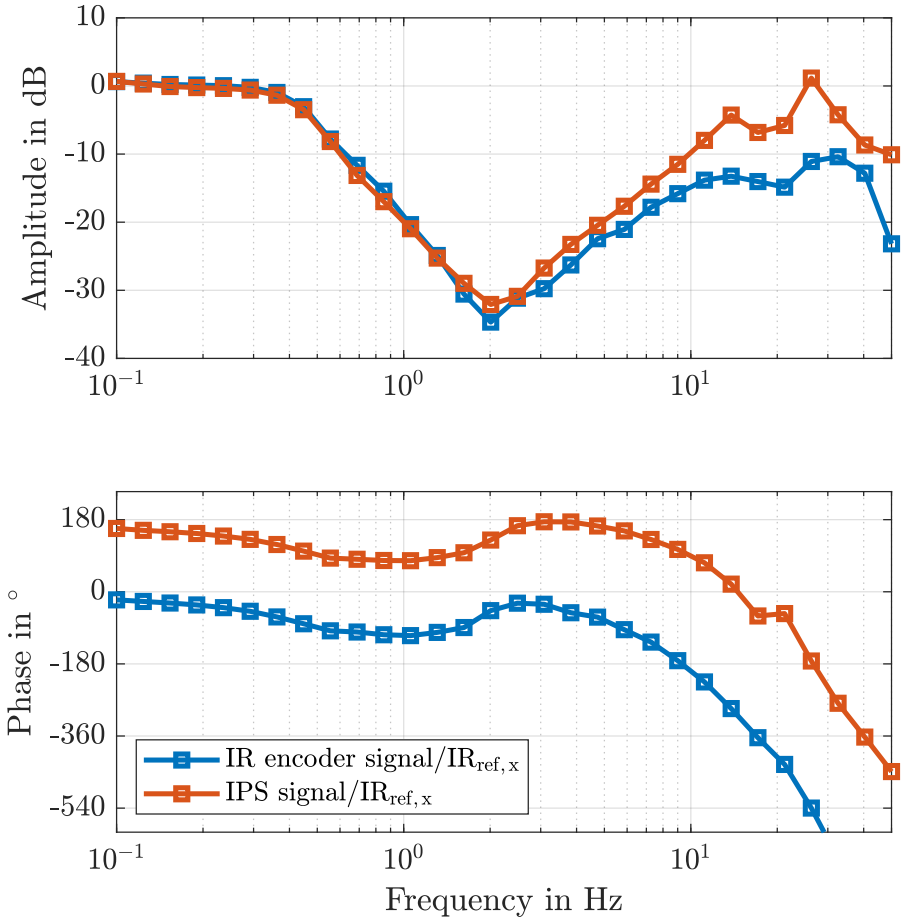

Figure 5.4: Identification of the robot dynamics in the DoF x measured by the IR encoder and IPS signal of the MP. For frequencies below 2 Hz magnitudes are measured similarly. The expected phase shift of 180 Hz between both signals is measured and the resonance peak at 26.8 Hz is not detected correctly by the IR encoder.

As mentioned earlier in this section, the IR dynamics will vary for different IR poses. Therefore, the dynamics are identified in three certain poses as shown in Figure 5.1. At each location, the dynamics of each DoF are identified separately, which are summarized in Figure 5.5. As can be seen for the DoFs y, z, ϕ_x, ϕ_y and ϕ_z the dynamics are only slightly changing along the conveyor system travel range. The identification of the DoF x shows that the dynamics differ for frequencies above 2 Hz for the different poses, which may have to be considered in the subsequent

control design. The analysis of the IR dynamics at different poses further shows

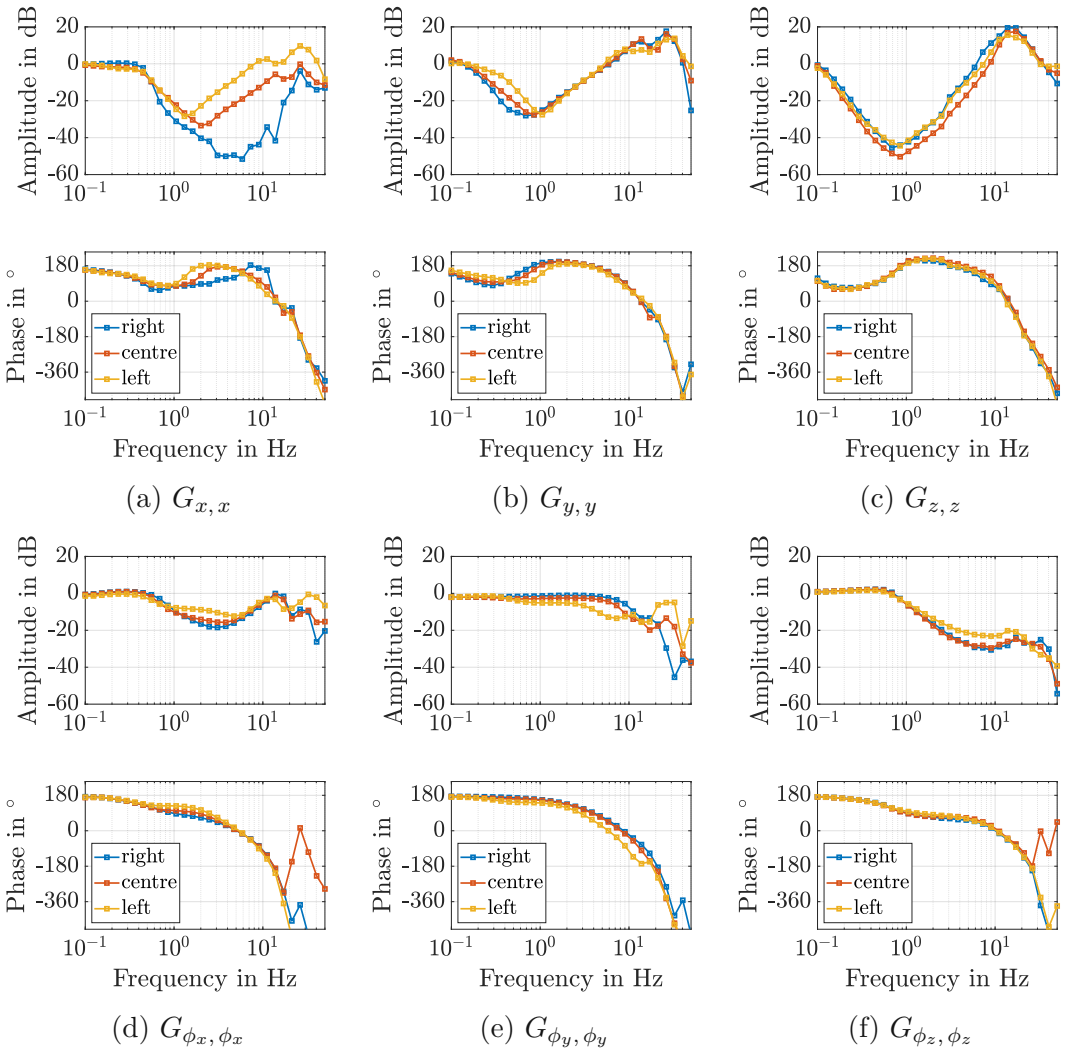

(a) $G_{x,x}$ (b) $G_{y,y}$ (c) $G_{z,z}$

(d) G_{ϕ_x,ϕ_x} (e) G_{ϕ_y,ϕ_y} (f) G_{ϕ_z,ϕ_z}

Figure 5.5: Identified dynamics of the IR in each DoF at the right and left end as well as in the centre of the conveyor travel range. A pair of anti-resonance and resonance are identified in each DoF in a frequency range of 0.6 to 6 Hz and 13 to 27 Hz for the anti-resonance and resonance, respectively. The DoF x shows slightly different dynamics along the travel distance of the conveyor system.

a pair of anti-resonance and resonance for all DoFs in a frequency range of 0.6 to 6 Hz and 13 to 27 Hz for the anti-resonance and resonance, respectively. The most probably cause of these pairs of anti-resonance and resonance is that IRs use flexible gear reducers, which allow high gear reduction ratios [71]. Such indirect drive mechanism can be modelled as a two mass system with a certain spring and

damping constant [72]. The author in [73] presents a precise analysis for a harmonic drive gear (flexible gear reducer) and identifies the dynamics of the FANUC M-16iB IR in a frequency range from 1 Hz to 100 Hz. The resulting system dynamics for each joint shows pairs of anti-resonances and resonances in a similar frequency region as the identified dynamics in Figure 5.5.

In a next step, the crosstalk is separately analysed for each translational and rotational DoF. The results related to this investigation are presented in Figure 5.6. It can be seen that for the DoF z the crosstalk is already significant for frequencies higher than 0.1 Hz, which may have to be considered in the subsequent control design. For the DoF x the crosstalk induced by a motion in DoF z is below 10 dB for frequencies up to 0.5 Hz (Figure 5.6a). The DoF ϕ_z (Figure 5.6f) shows a good decoupling from the other rotational DoFs (about 45 dB), whereas the DoF ϕ_x (Figure 5.6d) and DoF ϕ_y (Figure 5.6e) already show significant crosstalk for frequencies above 0.3 Hz and 0.2 Hz, respectively. The good decoupling of DoF ϕ_z is caused by the fact that only the IRs last joint (A6 in Figure 4.3) has to be actuated for a motion in DoF ϕ_z.

5.2 Control design for robust IR repositioning

In the following motion control concepts are introduced and designed to reposition the IR's TCP based on the identified IR dynamics of the previous section.

5.2.1 Feedback control for dual stage actuated system

In this section, the design of the targeted feedback control for the IR repositioning to enable the long-range tracking of a sample moved by the conveyor system is discussed. As described in Section 3.1, the MP compensates relative motion of the sample in tracking mode, which leads to a relative displacement of the MP out of its centre position. In order to ensure sufficient range for the MP to compensate low frequent relative motions, a feedback control for repositioning the IR to maintain the MP in its centre position is designed, based on the identified IR dynamics in the previous section. Therefore, the RSI is configured in relative cartesian correction mode, which allows to reposition the TCP of the IR in a cartesian coordinate system.
As described in Section 4.2.1, this interface operates at a cycle time of 4 ms. This means correction values are received and processed by the RSI cyclically in real-time. In order to investigate how the received correction values are processed by the RSI, a correction value of 10 µm is applied for one and two cycles, respectively, in the DoF x and the response of the robot motion is monitored (Figure 5.7). In

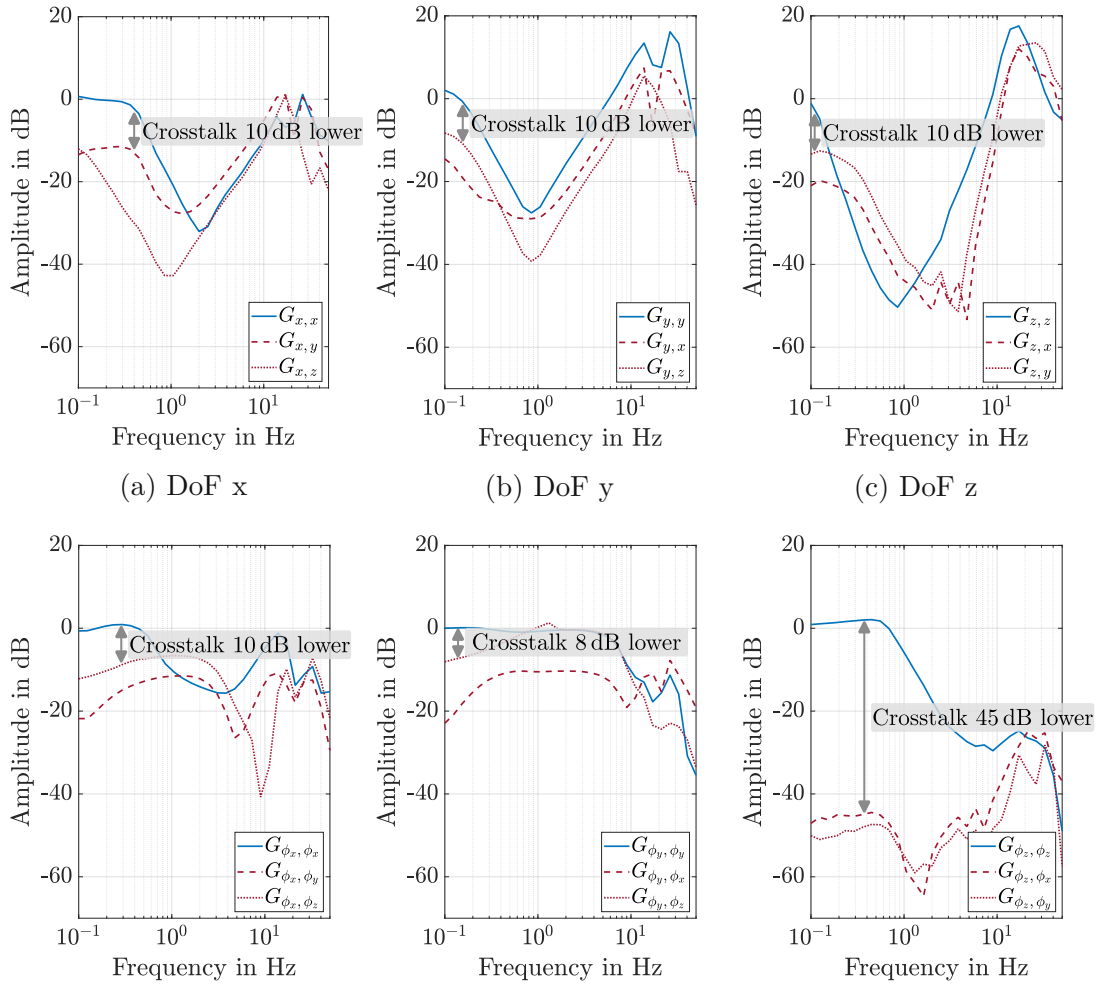

(a) DoF x (b) DoF y (c) DoF z

(d) DoF ϕ_x (e) DoF ϕ_y (f) DoF ϕ_z

Figure 5.6: Analysis of the identified crosstalk between the translational and rotational DoFs. For the DoF x, the crosstalk induced by a motion in DoF z is about 10 dB for frequencies up to 0.5 Hz. The DoF ϕ_z shows a good decoupling from the other rotational DoFs (about 45 dB), whereas the DoF ϕ_x and DoF ϕ_y already show significant crosstalk for frequencies above 0.3 Hz and 0.2 Hz, respectively.

Figure 5.7a it can be seen that for a single impulse applied to the RSI, it takes the IR about 2.5 s to perform the targeted motion of 10 µm. In comparison, Figure 5.7b shows the behaviour of the RSI, for the same correction value being applied for two cycles. A motion of 20 µm is performed within a time of 2.5 s. This is most probably caused by the fact that the RSI is queueing the received correction values internally and dynamically calculates the relative motion to be performed.

In addition, a time delay of 40 ms is identified in both scenarios, as can be seen in Figure 5.7c and 5.7d. In this time the robot is not moving at all. When designing

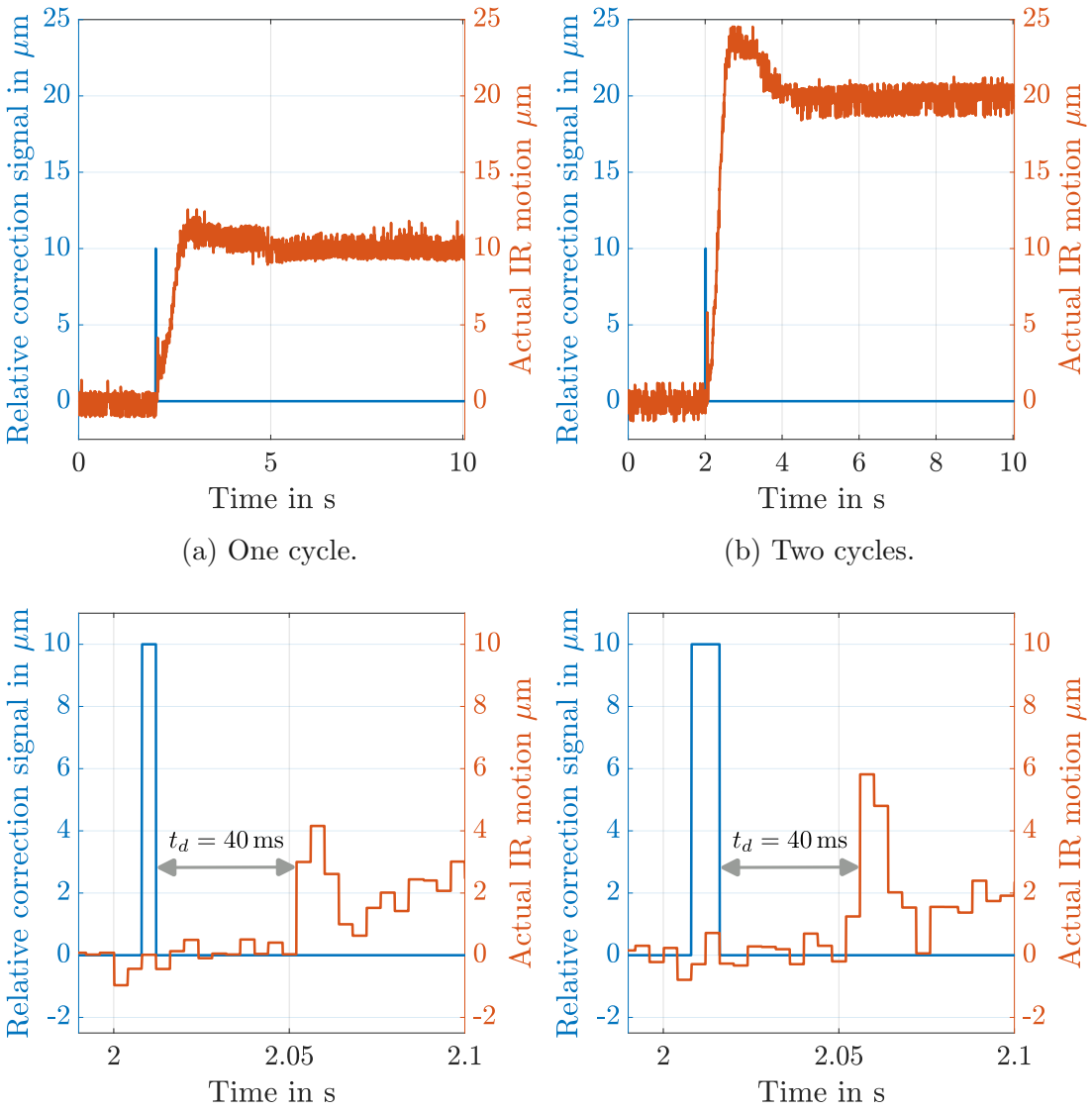

(a) One cycle.

(b) Two cycles.

(c) One cycle zoomed.

(d) Two cycles zoomed.

Figure 5.7: Response of the IR to an applied correction signal of 10 µm. In (a) and (b) the robot motion is plotted for a correction signal of 10 µm send over one and two RSI cycles, respectively. If the correction value is hold for two cycles, the total correction motion performed by the IR is twice as high. A time delay of $T_d = 40\,\text{ms}$ is identified, before the IR starts moving after a correction signal is applied ((c)-(d)).

a control for the repositioning of the IR, the queueing of the transmitted correction values by the RSI and the time delay need to be considered.
This problem can be best described in detail by a short example. Assuming a proportional robot control with $k_p = 1$ and an internal MP position error of 10 µm is present, the control task, described in Section 4.2.2, applies in each cycle ($T_s = 4$ ms) a correction value of 10 µm to the RSI. Due to the time delay of 40 ms, a total correction of 100 µm results, which is a factor of 10 higher than the initial correction value required, before the IR has even moved. Since the actuation range of the MP is limited, as described in Section 3.1, and in combination with the identified overshoot, as illustrated in Figure 5.7a and 5.7b, the repositioning of the IR by 100 µm can already lead to a violation of the mechanical limitations of the MP, which may damage the MP. To tackle this challenge, a delta error $\Delta e_{IPS,k} = e_{IPS,k} - e_{IPS,k-1}$ is introduced, which cyclically calculates the change of the error, as shown in Figure 5.8. However, this approach has the drawback that the information of the reference is lost. In order to push the error $e_{IPS,k}$ to zero, the error signal e_{IPS} is in addition averaged by using a lowpass filter with a 3 dB cut-off frequency of 10 Hz, resulting in $\bar{e}_{IPS}$. This signal is added for one cycle to the Δe_{IPS} signal, resulting in $\tilde{e}_{IPS,k} = \Delta e_{IPS} + \bar{e}_{IPS,k}$, if $\bar{e}_{IPS}$ exceeds the defined tolerances $tol_{\bar{e}}$ of 10 µm and 40 µrad for the translational and rotational DoFs, respectively. In order to provide the IR control unit enough time to perform the motion, a hysteresis of 100 cycles is applied. With this approach, the internal MP position error is kept within the tolerance $tol_{\bar{e}}$, which is sufficient with consideration of the MP's actuation range.
Based on the presented approach, a single input single output (SISO) control structure for the repositioning of the IR is synthesized, justified by the identified crosstalk being more than 8 dB lower in each DoF in the lower frequency range. Therefore, a discrete PID control

$$u(k) = k_p \left(\tilde{e}_{IPS,k} + \frac{T_s}{T_i} \sum \tilde{e}_{IPS,k} + \frac{T_d}{T_s} \tilde{e}_{IPS,k} \right) \tag{5.3}$$

is selected, with k_p being the proportional gain, and T_i, T_d the integrator and differentiator time constant, respectively. In addition, notch filters

$$H_{notch,i}(s) = \frac{s^2 + 2\delta\pi\nu + 4\pi^2\nu^2}{s^2 + 2\delta\rho\pi\nu + 4\pi^2\nu^2} \quad i = x,\, y,\, z,\, \phi_x,\, \phi_y,\, \phi_z \tag{5.4}$$

with δ defining the width and ρ the depth at a certain frequency ν are included in the control design (Figure 5.8) for each DoF to avoid excitation of the identified resonances in Section 5.1. The notch filter as well as the PID controller are designed in the time continuous domain and discretized with a sampling time $T_s = 4$ ms. The resulting controller in each DoF is as follows:

$$C_i(s) = C_{PID,i}(s) H_{notch,i}(s) \quad i = x,\, y,\, z,\, \phi_x,\, \phi_y,\, \phi_z \tag{5.5}$$

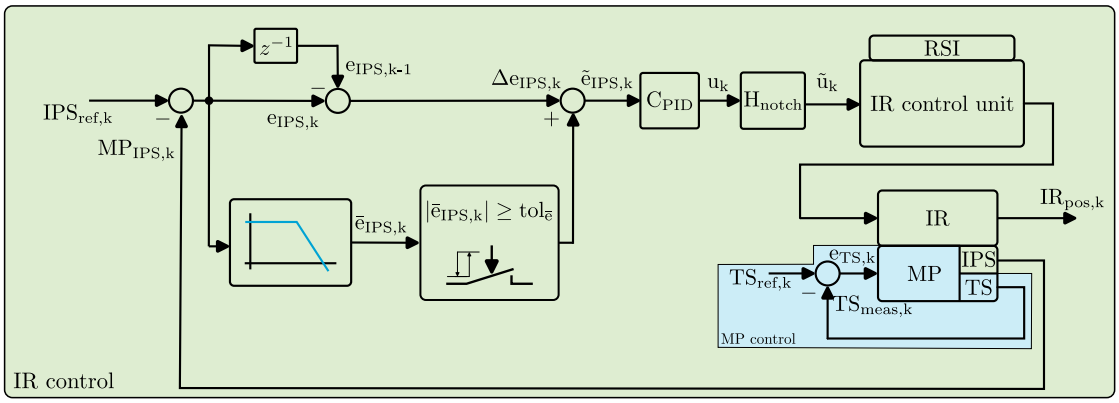

Figure 5.8: Block diagram of the feedback control for the IR repositioning to enable long-range tracking of a sample on a conveyor system. A delta error $\Delta e_{IPS,k} = e_{IPS,k} - e_{IPS,k-1}$ is calculated in each cycle to consider the queueing of applied correction values to the RSI. If a lowpass filtered error $\bar{e}_{IPS}$ exceeds the tolerance $tol_{\bar{e}}$ of 10 µm and 40 µrad for the translational and rotational DoFs, respectively, the error $\bar{e}_{IPS}$ is added for one cycle to the $\Delta e_{IPS,k}$. A hysteresis of 100 cycles is applied to provide the IR sufficient time to perform the motion. The error $\tilde{e}_{IPS,k}$ is proceeded by the PID control, resulting in the control output u_k. A notch filter is designed at the respective resonance frequency of each DoF. The resulting signal $\tilde{u}_k$ is applied to the IR control unit for repositioning the IR's TCP accordingly. The active sample tracking control of the MP is illustrated in the blue area.

with $C_{PID,i}$ being the respective implementation of the PID controller in the s-domain.
The control synthesis is exemplary shown for the DoF x. As described in Section 5.1, the IR dynamics of the DoF x is changing along the travel range of the conveyor system. For that reason, a controller is designed that is capable of operating robustly for the right and left end position of the conveyor system (Figure 5.1). A notch filter $H_{notch,x}$ is designed at 26 Hz with $\delta = 10$ and $\rho = 0.03$ to reduce the excitation of the antiresonance. In Figure 5.9 the system dynamics are shown for the left (solid) and right (dashed) position. The control parameters of Equation 5.3 are synthesized in a loop-shaping approach. Therefore, k_p is increased and T_i is decreased, until a phase margin below 20 ° is obtained. The differentiator time constant is defined in the end to slightly increase the phase at the the cross-over frequency. With the resulting parameters $k_p = 1.5$, $T_i = 0.25$ and $T_d = 0.6$, a robust design for the two IR extreme poses is obtained. The loop gain for the left ($L_{x,left}$) and right pose ($L_{x,right}$) shows a resulting gain and phase margin of 8 dB/50 dB and 40 °/20 °. The corresponding cross-over frequencies of the loop

gain in both IR extreme poses is 0.55 Hz.
This scheme is repeated for the other DoFs. In Table 5.1, the resulting control

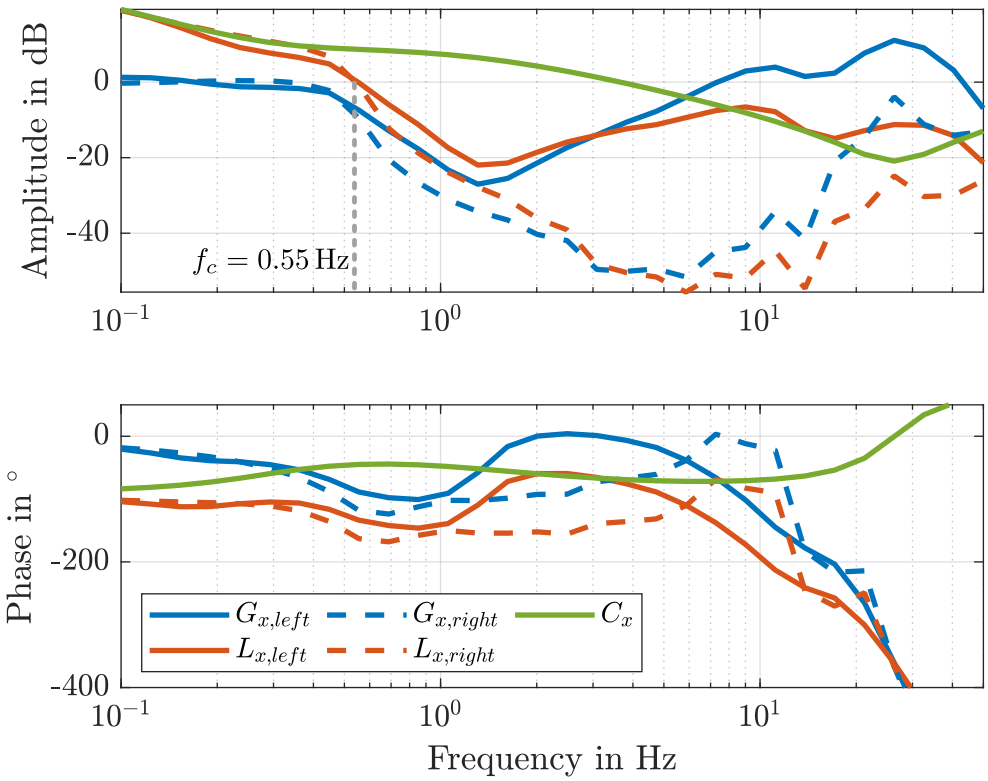

Figure 5.9: Control design for the repositioning of the IR at both extreme poses in DoF x. A cross-over frequency of 0.55 Hz is designed for both loop gains ($L_{x,left}$ and $L_{x,right}$), with a resulting gain and phase margin of 8 dB/50 dB and 40 °/20 ° for the left ($L_{x,left}$) and right pose ($L_{x,right}$). The dynamics C_x is the combination of the PID and notch filter dynamics.

parameters, with the corresponding cross-over frequencies, as well as phase and gain margins are summarized. Figure 5.10 shows for each DoF the system dynamics $G_{i,centre}$ of the IR, the designed controller dynamics $C_{i,centre}$ the tailored notch filter, designed and the resulting open-loop gain $L_{i,centre}$. Since the dynamics for the other DoFs is staying in a good approximation the same along the travel-range of the conveyor system, the controllers are designed for the IR dynamics in the centre position. As the sample motion direction is limited by design to the translational DoF x, lower cross-over frequencies for the loop gains in the other DoFs can be designed. For that reason, a PI control structure is sufficient to achieve phase margins beyond 50 °.

Table 5.1: Summary of the control parameters for the IR repositioning with the corresponding crossover frequencies and phase/gain margins for each DoF in centre position of the conveyor travel range.

Axis	k_p	T_i	T_d	Crossover frequency f_c in mHz	Phase margin in °	Gain margin in dB
x	1.5	0.25	0.6	550	46	14
y	0.9	0.8	0	180	60	5.5
z	0.1	5	0	105	55	12
ϕ_x	0.9	1.4	0	340	113	23
ϕ_y	0.9	1.2	0	135	124	12
ϕ_z	0.7	1.5	0	140	128	40

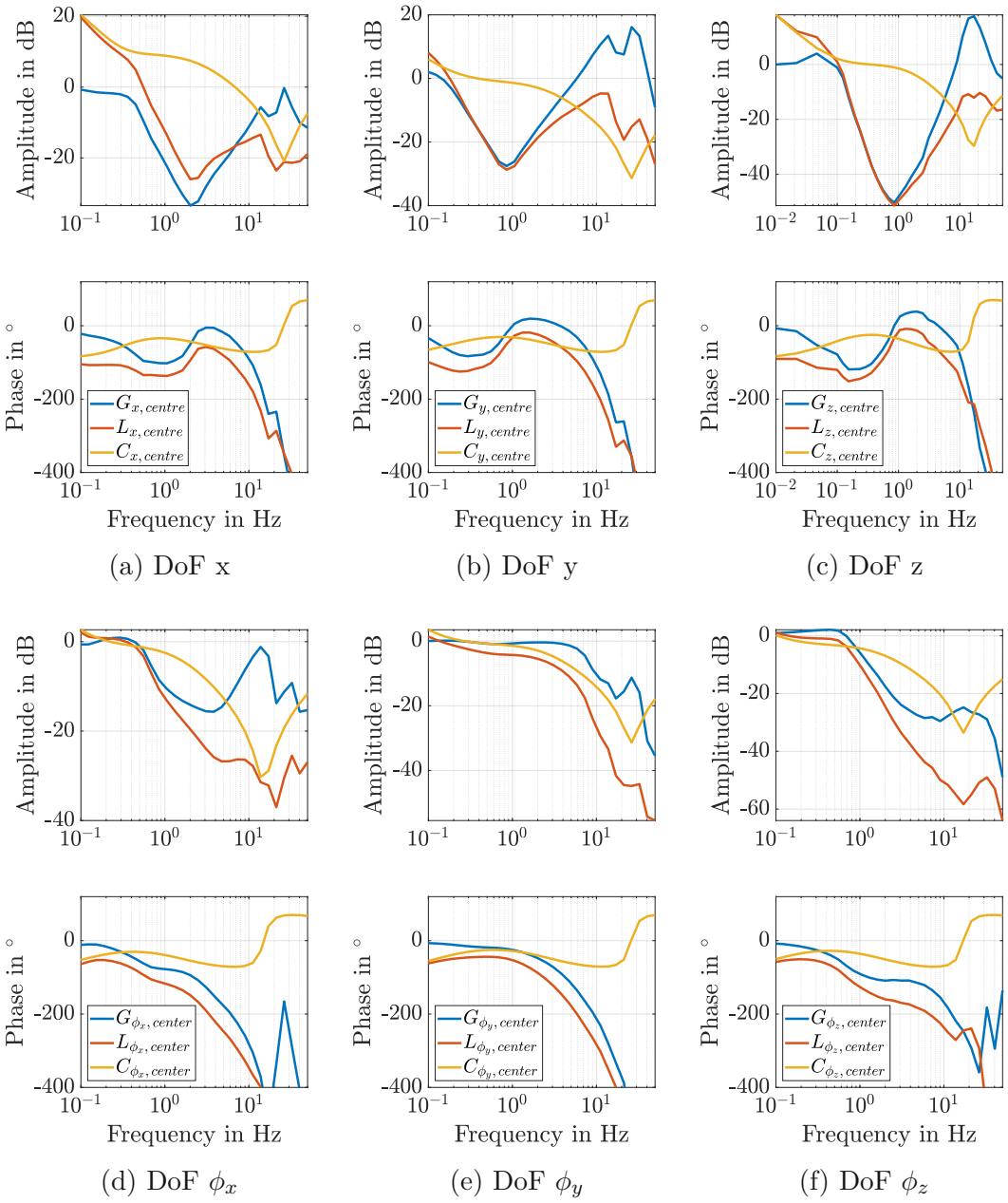

(a) DoF x (b) DoF y (c) DoF z

(d) DoF ϕ_x (e) DoF ϕ_y (f) DoF ϕ_z

Figure 5.10: Control design for repositioning the IR in each DoF in the centre position of the conveyor travel range. The measured IR dynamics $G_{i,centre}$, the resulting loop gain $L_{i,centre}$ for the designed controller $C_{i,centre}$, which is a combination of the PID controller and notch filter are shown.

5.2.2 Feedforward control for dual stage actuated system

In order to further improve the IR repositioning performance, the up-front known conveyor velocity is used as *a priori* knowledge in a feedforward scheme. Therefore, a feedforward path is added to the feedback loop introduced in the previous section, as shown in Figure 5.11. The actual conveyor velocity is therefore multiplied by the cycle time of 4 ms, represented by the factor k_{conv} in the block diagram. In this way, the cyclically calculated positioning error should be decreased hence, reducing the feedback control effort and increasing the overall system performance.

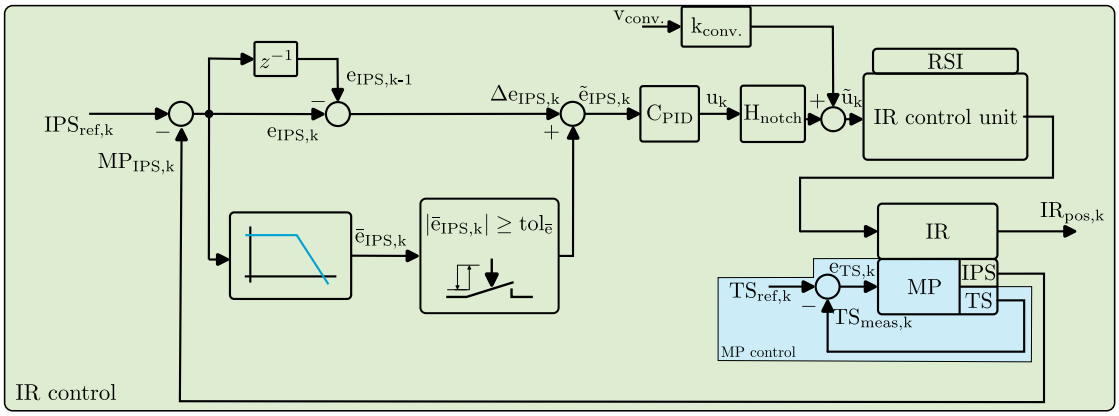

Figure 5.11: Block diagram of the combined feedforward and feedback control for the IR repositioning to enable long-range tracking of a sample on a conveyor system. The control structure presented in Figure 5.8 is extended by including the *a priori*-known conveyor velocity, which gets multiplied by a constant gain $k_{conv} = 4\,\text{ms}$, to convert the velocity signal into a corresponding position signal. The resulting signal $\tilde{u}_k$ is applied to the IR control unit for repositioning the IR accordingly. The active sample tracking control of the MP is illustrated in the blue area.

CHAPTER 6

Experimental evaluation of the system performance

This chapter evaluates the performance of the dual stage-controlled robotic system for inline 3D measurements on moving objects. Firstly, the measurement setup is described in detail. Next, the designed and implemented control architectures described in Chapter 5 are evaluated regarding performance and robustness. Finally, the achieved 3D imaging performance on a moving sample is determined.

6.1 Measurement setup and sample motion trajectories

To evaluate the performance of the dual stage-controlled robotic system for inline 3D measurements on moving objects, the industrial robot (IR) is positioned such that the measurement platform (MP) is placed at the right end of the conveyor system above the sample box, with the tracking sensors (TSs) being in range (Figure 6.1). The coordinate system of the MP tool center point (TCP) defines the corresponding correction directions of the IR, as described in Section 5.1, whereas the sample motion is performed along the degree of freedom (DoF) x. A velocity profile with the corresponding acceleration shown in Figure 6.2 is applied to the conveyor system. In this trajectory, the acceleration time (t_{acc}) and the plateau velocity (v_{sample}) can be set variably, which allows to distinguish between two sectors for the following performance evaluation. The sector, where the acceleration is unequal to zero is used to determine the IR control performance. The sector, in which the acceleration is zero, is used to identify the tracking performance of the MP as well as the 3D imaging performance on a moving sample. Throughout this

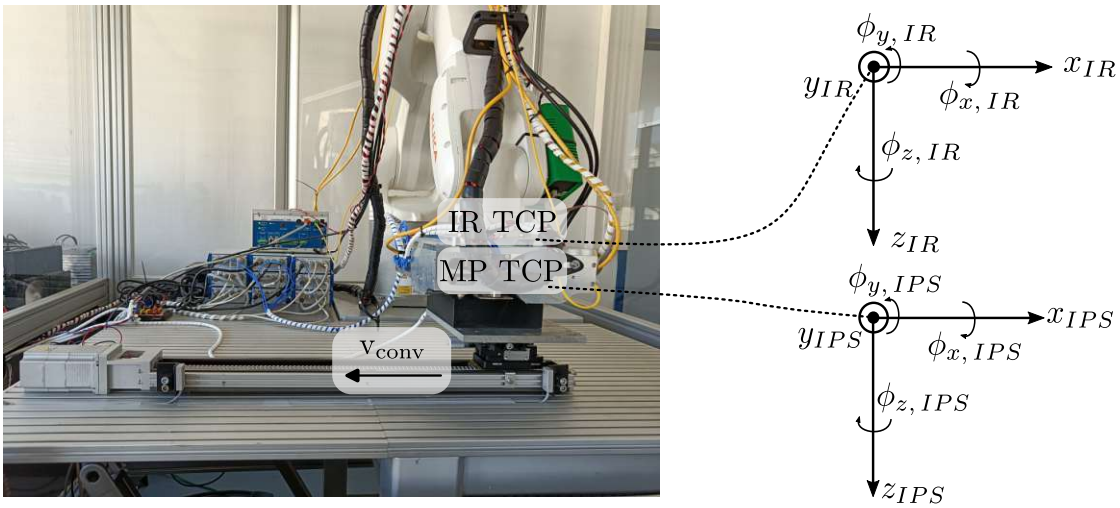

Figure 6.1: Measurement setup to evaluate the system performance. The IR pose is adjusted such that the TSs of the measurement module are placed well within their actuation range above the sample box. The start point for the performance evaluation is the right end of the conveyor system. The coordinate systems of the MP and the IR illustrate the orientation of each TCP accordingly. The motion direction is along the x-axis. The conveyor velocity v_{conv} can be precisely adjusted for the different performance evaluation steps.

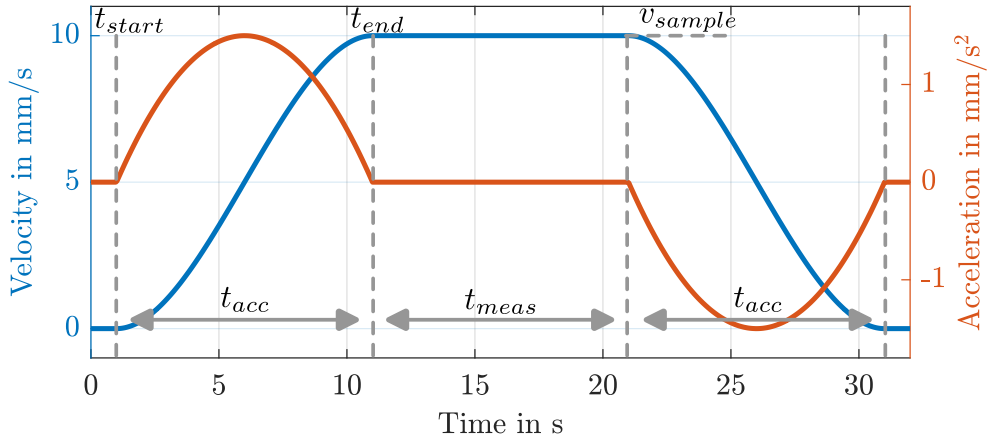

Figure 6.2: Applied velocity trajectory with its corresponding acceleration profile. The acceleration time t_{acc} and plateau velocity v_{sample} can be adjusted. The measurement time t_{meas} is set to 10 s.

chapter, this sector is stated as measurement section.
The measurement time t_{meas} is set to 10 s, which allows to gather 3D images with

appropriate resolution as described in [20]. Combinations of the acceleration times and velocities v_{sample}, as shown in Table 6.1, are used throughout the subsequent investigations to evaluate the entire system performance. Considering the targeted sample speeds defined in Section 1.2, velocities up to 10 mm/s are evaluated in the following.
The velocity trajectory starting at 0 mm/s to the desired sample velocity v_{sample}, is dynamically calculated based on a third order polynomial function

$$v_{conv} = v_1 t^3 + v_2 t^2 + v_3 t + v_4 \tag{6.1}$$

where v_1 to v_4 notate the polynomial coefficients and are determined by the following constraints:

$$v(t_{start}) = 0 \tag{6.2}$$
$$v(t_{end}) = v_{sample} \tag{6.3}$$
$$\dot{v}(t_{start}) = a(t_{start}) = 0 \tag{6.4}$$
$$\dot{v}(t_{end}) = a(t_{end}) = 0 \tag{6.5}$$

with t_{start} defining the time stamp at which the trajectory is applied and t_{end} results based on the desired acceleration time t_{acc}. The reason for selecting a third-order polynomial velocity trajectory is based on a trade-off between peak acceleration in the mid and jerky motion at the start as well as at the end of the sample motion to be tracked.

Table 6.1: Overview of the applied acceleration times and sample velocities v_{sample} throughout the performance evaluation.

Acceleration times in s	0.1	0.3	0.5	0.7	1	2	4	6	8	10
v_{sample} in mm/s	0.5	1	3	5	7	9	10			

6.2 Dual stage-controlled IR repositioning

In the following the performance of the introduced control concepts in Section 5.2 to reposition the IR on the long-range are evaluated.

6.2.1 IR repositioning without *a priori* knowledge

In a first step the feedback control performance, designed in Section 5.2.1, to reposition the IR to enable the long-range tracking of a sample moved by the

conveyor system is evaluated, without knowledge of the actual sample velocity.

Considering the velocity trajectory in Figure 6.2, the minimum acceleration time t_{acc} for a certain plateau velocity v_{sample} is identified, for which the MP is maintained within its defined safe range (see Section 3.1). For this performance evaluation the measurement time t_{meas} is reduced to 2 s, in order to enable higher velocities to be tracked along the limited travel range of 400 mm of the conveyor system. As the motion direction is along the DoF x, the internal MP position error in DoF x serves as the performance indicator. The results related to this evaluation are summarized in Table 6.2.

Table 6.2: Comparison of the experimentally evaluated IR repositioning performance without *a priori* knowledge of the conveyor system.

v_{sample} in mm/s	Acceleration time t_{acc} in s	max. acceleration in mm/s^2	max. internal MP position error in DoF x in µm	Travelled sample distance in mm
0.5	4	0.19	97.5	3.16
1	8	0.19	107.3	10.31
2	20	0.15	102.9	44.91
3	30	0.15	108.3	97.14
4	50	0.12	109.9	208.31

As can be seen in Table 6.2 a velocity v_{sample} of 0.5 mm/s is achievable within an acceleration time t_{acc} of 4 s. A peak acceleration of 0.19 mm/s^2 is determined, yielding an internal MP position error of 97.5 µm, which is 25 µm less then the safety limitation of the MP (see Section 3.1). To obtain higher sample velocities v_{sample}, the acceleration time t_{acc} needs to be increased. A velocity $v_{sample} = 4$ mm/s is reached within an acceleration time of 50 s. This leads to an experimentally determined peak acceleration of 0.12 mm/s^2.
Figure 6.3 exemplary shows the measured internal MP position error for the translational and rotational DoFs for a velocity $v_{sample} = 3$ mm/s and an acceleration time of 30 s. As shown, the internal MP position error in the motion direction x is continuously increasing within the acceleration phase reaching the peak error of 108.27 µm at the point of maximum acceleration. From that point on, the error is decreasing until the sample gets decelerated from $v_{sample} = 3$ mm/s back to zero, where the internal MP position error starts to increase again. The high frequent noise in the internal MP position signals in Figure 6.3b and 6.3c represents the

tracking motion of the MP, which is required to establish the stiff link between the scanning confocal chromatic sensor (SCCS) on the MP and the sample. As can be seen from the evaluated translational internal MP position error root mean square (RMS) values (Figure 6.3b), the control action of the MP is highest for the DoF x, resulting in an RMS value of 50.82 μm.
Figure 6.4a to 6.4c show accordingly the performed IR motion in each DoF for the experiment in Figure 6.3. For the given velocity trajectory, as shown in Figure 6.3a, the IR travels 97.41 mm in total in the motion direction (DoF x). Throughout this travel distance, the altitude changes by 0.94 mm. By analysing the motion in the DoF ϕ_x it can be concluded that the conveyor system shows slight tilt.

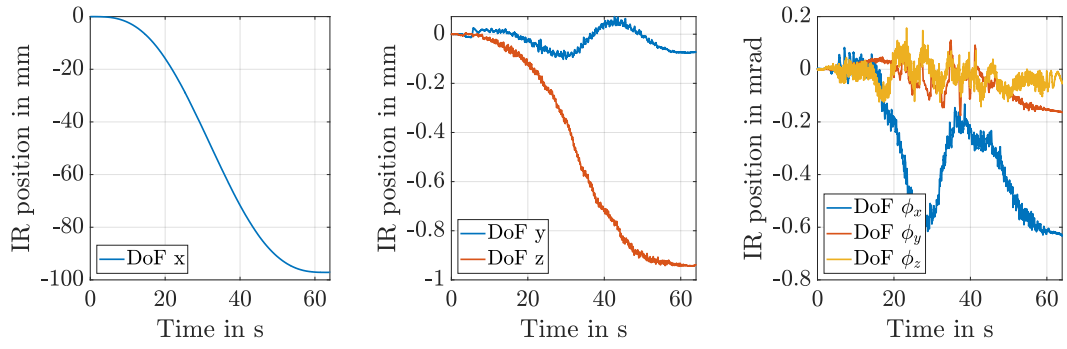

Figure 6.4: Performed IR motion without *a priori* knowledge of the conveyor velocity in each DoF for the applied velocity trajectory with a sample velocity $v_{sample} = 3\,\text{mm/s}$ and an acceleration time of 30 s. (a) shows the in total travelled distance of 97.14 mm by the IR in motion direction (DoF x) along the conveyor travel range. In (b), the performed motion for the DoFs y and z are illustrated. A change in altitude of 0.94 mm and a curvy motion in DoF y are visible along the travel distance of the conveyor. The performed rotational motion by the IR is shown in (c).

Summing up, without *a priori* knowledge of the conveyor motion a robust repositioning of the IR for velocities up to 4 mm/s is demonstrated and sample accelerations of up to 0.12mm/s^2 can be robustly tracked.

6.2.2 IR repositioning with *a priori* knowledge

The results of the previous section show that the dual stage-controlled IR repositioning is limited to accelerations of $0.12\,\text{mm/s}^2$. In a next step the performance gain by using *a priori* knowledge of the actual sample velocity for the control of repositioning

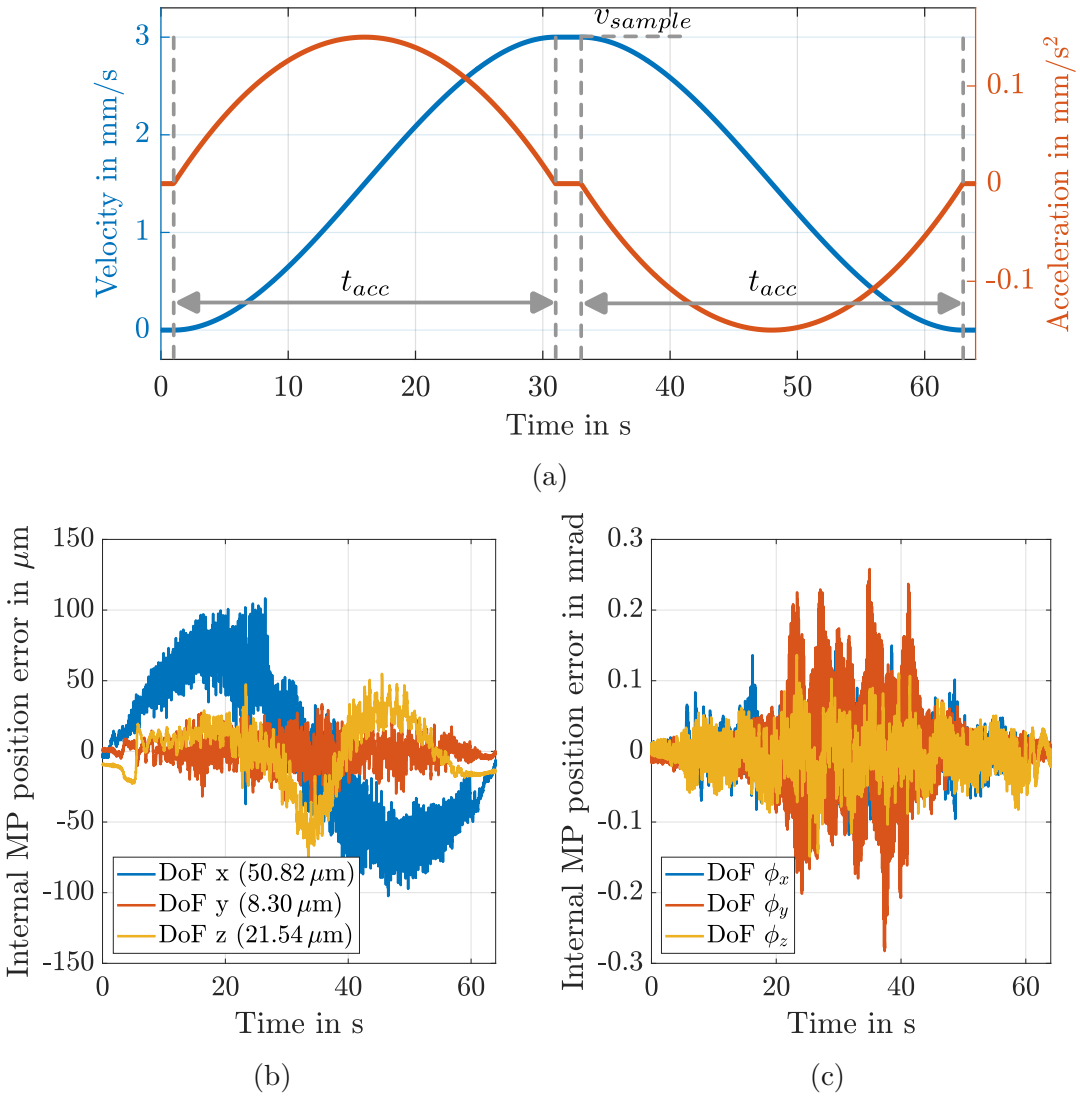

Figure 6.3: Performance evaluation of the dual stage-controlled IR without *a priori* knowledge. (a) shows the applied velocity trajectory with a sample velocity v_{sample} of 3 mm/s achieved within an acceleration time of 30 s, with a peak acceleration of 0.15 mm/s^2. The translational internal MP position errors, representing the MP's tracking motion, for the translational DoFs are illustrated in (b). In motion direction (DoF x), a peak error of 108.3 µm is measured during the sample acceleration between 1 and 31 s. The rotational internal MP position errors, stay within ±0.25 mrad and are illustrated in (c).

the IR to enable the long-range tracking of a sample is evaluated. For that reason,

the feedback control is extended, as described in Section 5.2.2 by a feedforward part.

The performance is identified by repeating the experiments from Section 6.2. The measurement time is set 10 s. Figure 6.5a shows the resulting peak accelerations for different velocities v_{sample} and acceleration times t_{acc}. Sample velocities v_{sample} of 0.5 and 1 mm/s are achieved within an acceleration time of 0.1 s, yielding peak accelerations of 7.5 mm/s^2 and 15 mm/s^2, respectively. Furthermore, a sample velocity $v_{sample} = 10$ mm/s can be reached within 2 s, where the maximum acceleration yields 7.5 mm/s^2. In Figure 6.5b, the internal MP position error is shown for the motion DoF x for different velocities v_{sample} and acceleration times t_{acc}. It can be seen that except for $v_{sample} = 0.5$ and 1 mm/s a decrease of the acceleration time for a given velocity leads to higher internal MP position errors. Figure 6.6

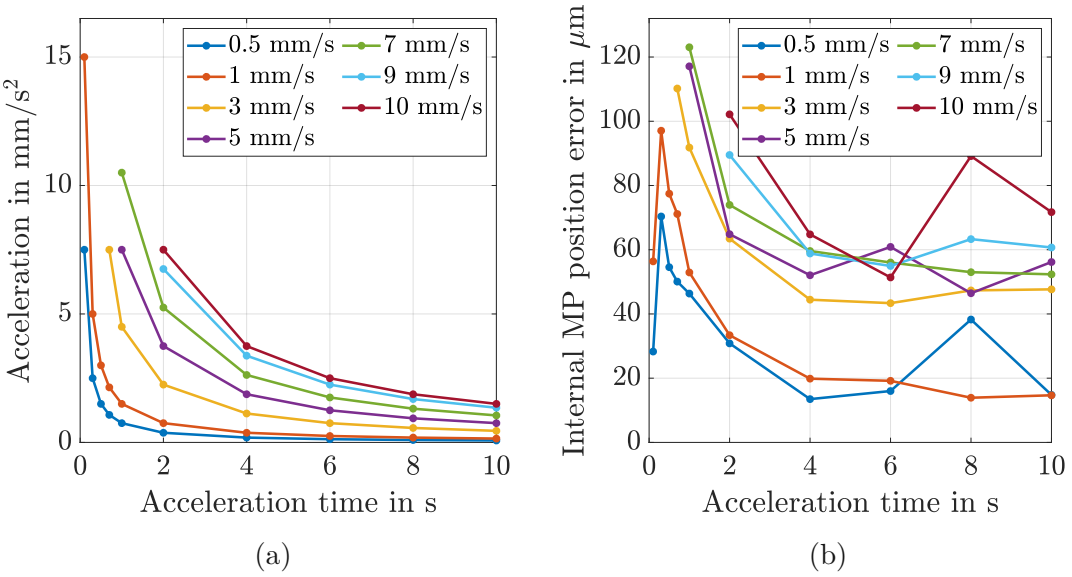

(a) (b)

Figure 6.5: Evaluation of the maximum achievable conveyor accelerations without exceeding the MP safety limitations. (a) compares the achievable maximum conveyor accelerations for different acceleration times and velocities v_{sample}. (b) shows the corresponding maximum internal MP position error in motion direction.

exemplary shows the internal MP position error for the translational and rotational DoFs for a velocity $v_{sample} = 10$ mm/s and an acceleration time of 2 s. It can be seen that during the acceleration phase the internal MP position error increases and reaches a peak value of 102 µm. Within the measurement section of the velocity trajectory, the internal MP position error is close to zero in average on each DoF. Figure 6.7 shows to the experiment in Figure 6.6 the corresponding IR motion in each DoF. For the applied velocity trajectory the IR travels in motion direction

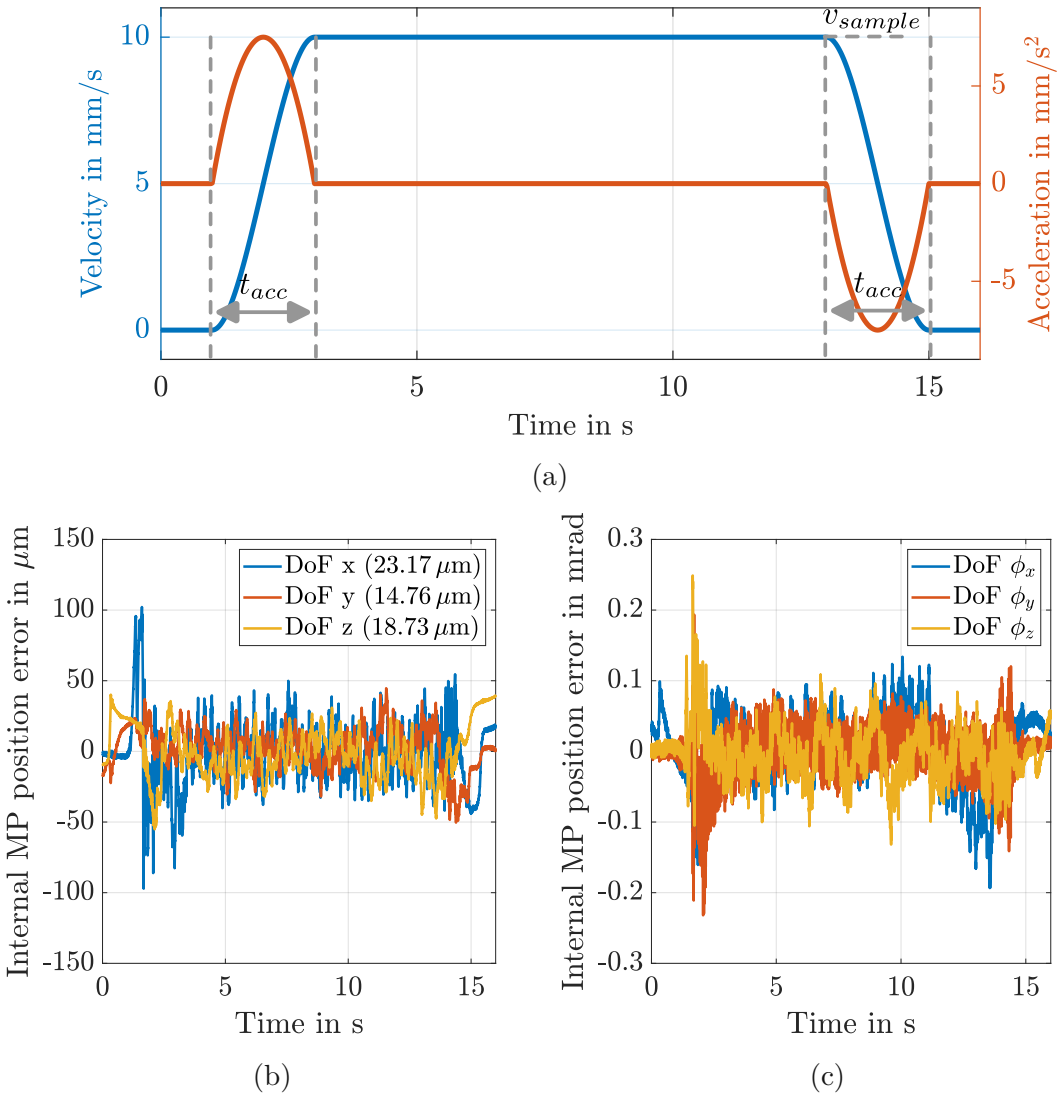

Figure 6.6: Performance evaluation of the dual stage-controlled IR with *a priori* knowledge. (a) shows the applied velocity trajectory with a sample velocity v_{sample} of 10 mm/s achieved within an acceleration time of 2 s with a peak acceleration of 7.5 mm/s^2. The translational internal MP position errors, representing the tracking motion, for the translational DoFs are illustrated in (b). In motion direction (DoF x) a peak error of 102 µm is measured during the sample acceleration between 1 and 3 s. The rotational internal MP position errors stay within ±0.25 mrad are illustrated in (c).

(DoF x) a total distance of 113 mm. Compared to the results in Section 6.2.1,

the use of *a priori* knowledge significantly decreases the required travel distance. Figure 6.7b and 6.7c indicates a similar IR motion in the other DoF, as discussed in Section 6.2.1.

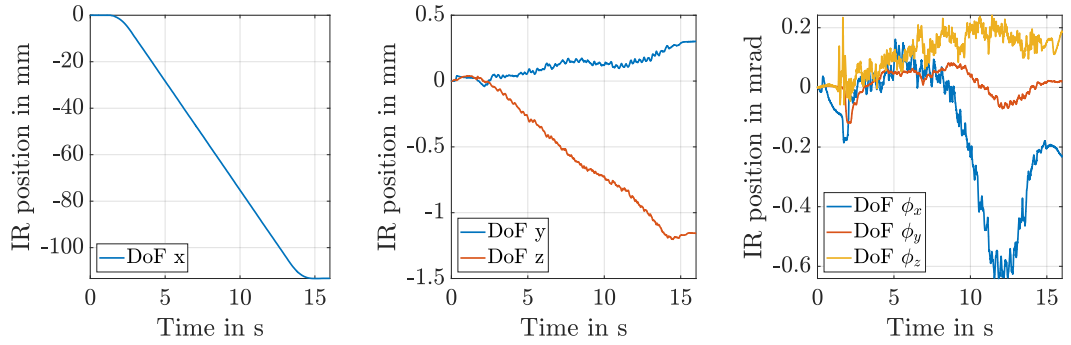

(a) (b) (c)

Figure 6.7: Performed IR motion with *a priori* knowledge of the conveyor velocity in each DoF for the applied velocity trajectory with a sample velocity $v_{sample} = 10\,\text{mm/s}$ and an acceleration time of 2 s. (a) shows the in total travelled distance of 113 mm by the IR in motion direction (DoF x) along the conveyor travel range. In (b) the performed motion for the DoFs y and z are illustrated. A change in altitude of 1.15 mm is visible along the travel distance of the conveyor. The performed rotational motion by the IR is shown in (c). A slight tilt placement and induced shakes by the conveyor itself can be seen in the DoF ϕ_x motion.

In summary, the use of *a priori* knowledge in the IR repositioning control significantly increases the performance of the dual stage-controlled robotic system. Maximum sample accelerations of $7.5\,\text{mm/s}^2$ for a velocity $v_{sample} = 10\,\text{mm/s}$ are reached, within an acceleration time of 2 s. As compared to the results without *a priori* knowledge of the conveyor system in Section 6.2.1, the performance of the system can be increased by a factor of 62.

6.3 Evaluation of the sample tracking performance in motion

In a next step, the system's long-range active sample tracking performance of a moving object is evaluated. Serving as a benchmark, the tracking control bandwith (BW) is reduced to 1 Hz in each DoF, emulating a measurement with disabled tracking control. Using this low BW controller, higher frequent disturbances are not suppressed. Again, the velocity profile presented in Figure 6.2 with different velocities v_{sample} is applied to the conveyor system. Within the measurement

interval t_{meas}, the RMS value of the tracking error for each translational DoF is determined. Next step, the tracking control BW is increased to its default value of 400 Hz and the measurements are repeated with the high performance tracking controller.
In Figure 6.8, the comparison between the low and high BW controller is exemplarily shown for a conveyor velocity of $v_{sample} = 10\,\text{mm/s}$. Figure 6.8a illustrates the applied velocity trajectory to the conveyor system, while Figure 6.8b and 6.8c analyse the tracking error in motion direction (DoF x) and in the out-of-plane DoF z. As shown, the high BW tracking controller reduces the relative motion between the MP and the sample to the sub-micrometre scale, with residual tracking errors of 486 nm rms and 167 nm rms in motion direction and the translational out-of-plane DoF z, respectively.
Table 6.3 summarizes and lists the resulting tracking errors in the translational DoFs using the low and high BW tracking controllers during the measurement interval t_{meas} at different sample velocities v_{sample}.

Table 6.3: Comparison of the tracking error using the high and low BW tracking control at different sample velocities v_{sample}.

Conveyor system vel. in mm/s	Tracking error rms in μm x	y	z
Low bandwidth			
0.5	3.398	4.827	2.080
1	4.915	4.726	3.340
3	15.484	12.167	10.445
5	22.412	11.068	7.860
7	26.210	17.563	11.333
9	16.708	15.294	10.406
10	15.548	15.559	10.672
High bandwidth			
0.5	0.294	0.399	0.044
1	0.289	0.324	0.047
3	1.092	0.444	0.227
5	1.308	0.385	0.326
7	0.663	0.615	0.307
9	0.563	0.390	0.174
10	0.486	0.393	0.167

As can be seen in Table 6.3, using the low BW tracking controller, a relative motion

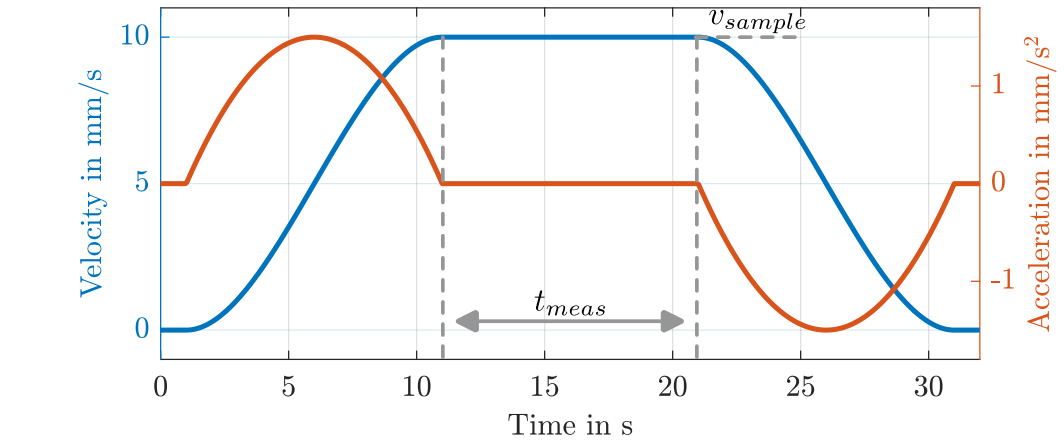

(a)

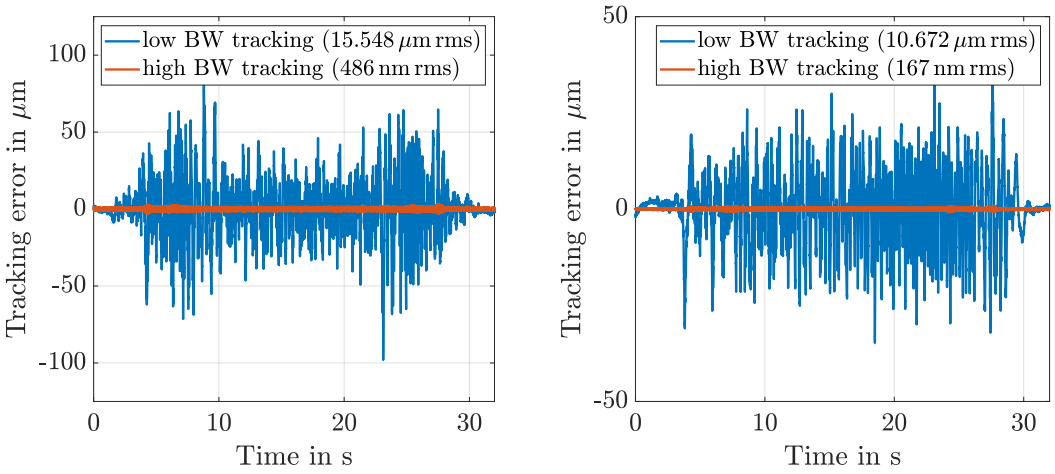

(b) DoF x.

(c) DoF z.

Figure 6.8: Tracking performance at $v_{sample} = 10\,\text{mm/s}$. Using the high BW tracking controller, the tracking error in motion direction (DoF x) and the out-of-plane DoF z is reduced to the sub-micrometre scale.

between the MP and the sample of up to 26.21 µm rms results during the sample motion. By enabling the high BW controller, this relative motion is reduced to the sub-micrometre range, except for DoF x (motion direction) at 3 and 5 mm/s. The increased residual tracking error at these velocities is caused due to excitation of the conveyor system structure. Figure 6.9 analyse the tracking error in motion direction (DoF x) at 5 and 10 mm/s. As can be seen, a structural mode with a frequency of 83.3 Hz at 5 mm/s is excited, whereas the tracking error at a velocity of 10 mm/s shows no such dominant component.

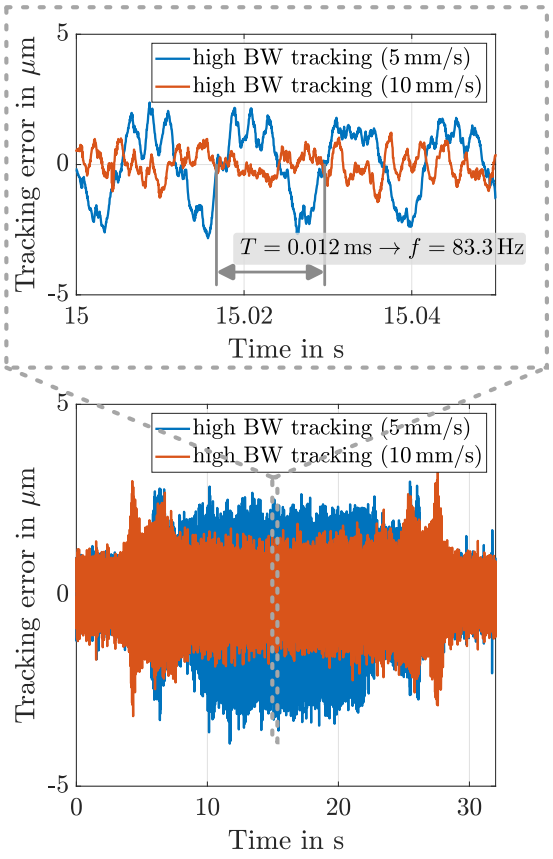

Figure 6.9: Detailed analysis of the tracking error at a conveyor velocity of 5 and 10 mm/s. At $v_{sample} = 5\,\text{mm/s}$, a structural mode of the conveyor system at 83.3 Hz is excited, resulting in an increased tracking error.

Table 6.4 summarizes the relative vibration rejection capability by using the high BW tracking controller in relation to the low BW tracking controller for the translational DoFs. At a maximum velocity of $v_{sample} = 10\,\text{mm/s}$, a vibration rejection of 96.88 % is achieved in motion direction (DoF x) and 98.44 % in the out-of-plane DoF z.
Summing up, the experimental results demonstrate the long-range precision sample tracking capability of the dual-stage-controlled robotic system. For sample motions with velocities of up to 10 mm/s, tracking errors on the sub-micrometer scale are achieved, actively compensating 97 % of disturbing relative motion between the MP and the sample.

Table 6.4: Summary of the relative vibration rejection capability of the high BW tracking control in relation to the low BW tracking control of the MP.

Conveyor system vel. in mm/s	Vibration suppression in %		
	x	y	z
0.5	91.35	91.73	97.88
1	94.11	93.14	98.58
3	92.95	96.35	97.83
5	94.16	96.52	95.86
7	97.47	96.50	97.29
9	96.63	97.45	98.33
10	96.88	97.48	98.44

6.4 Robotic precision 3D measurements on moving objects

With consideration of the system requirements in Section 1.2 and the research question defined in Section 2.4, the system's 3D imaging performance on a moving sample is evaluated in a next step. As a test sample surface, a calibration standard with 20 µm pitch and a structural height of 25 µm is selected and mounted on the sample box (see Figure 3.2b).
In Figure 6.10a, a microscope image of the selected region of interest is shown. As can be seen, the region of interest contains surface defects, which are most likely dust particles. Figure 6.10b shows the according 3D measurement by the SCCS in static lab conditions, i.e. the conveyor system as well as the IR are disabled and the sample tracking control is on, with a measurement time of 10 s. Note, that the structural height is not measured correctly, as the CCSs light spot diameter equals the structural width (10 µm) [64]. However, the surface defects are clearly visible in the the measurement result and the vertical line along the grating top at $y = 205$ µm is used as a benchmark for further investigations on the system performance. In a next step, the 3D imaging performance of the robotic measurement system is evaluated with the sample in motion. Applying the velocity trajectory presented in Figure 6.2, 3D measurements are performed separately using the low and high BW tracking control (see Section 6.3) at a plateau velocity of $v_{sample} = 1$ mm/s. The results are related to this experiment are presented in Figure 6.11a and 6.11b. As can be seen for the 3D measurement with the low BW tracking control, motion blur is corrupting the result, as the MP is not capable to establish the required stiff link between the SCCS and the sample. In contrast, the grating structure and the surface defects are clearly visible in the 3D measurement

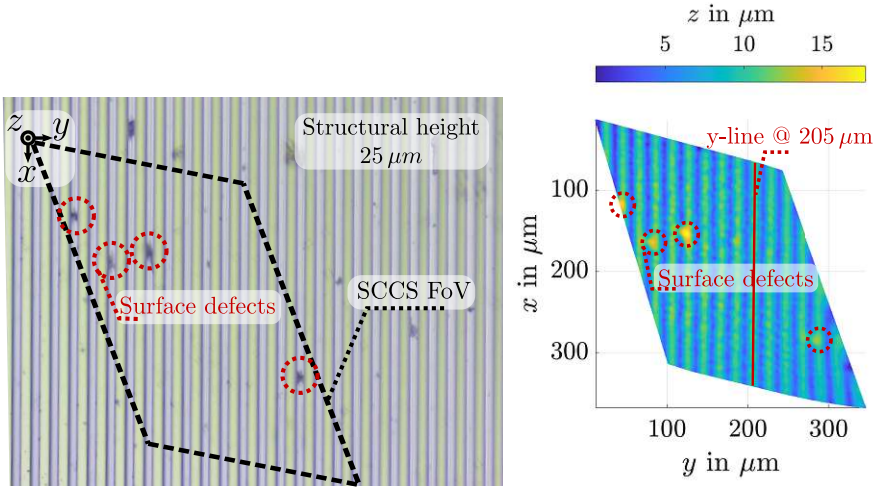

(a) (b)

Figure 6.10: Test sample structure for evaluating the 3D imaging performance. In (a), a microscope image of the calibration standard with 20 µm pitch and a structural height of 25 µm is shown, with some dust particles visible in the selected region of interest. (b) shows the according 3D measurement, which serves as a benchmark. The surface defects are clearly visible in the measurement result.

using the high BW tracking control (Figure 6.11b).
By analysing the cross section at $y = 205\,\mu m$ along the grating top, indicated by the red solid line in Figure 6.10b, 6.11a and 6.11b, the performance increase becomes even more clear. In the static case (benchmark), the z-ripple along the grating top is 584 nm rms. Using the low BW tracking control for measuring on the moving sample with 1 mm/s, this value is increased to 5.161 µm rms. By enabling the high BW tracking control, a z-ripple of 610 nm rms is achieved, boosting the 3D imaging performance by a factor of 9 to the same order of magnitude as obtained in the benchmark measurement.
Finally, the system performance is demonstrated and evaluated at sample speed of $v_{sample} = 10\,mm/s$. Therefore, the velocity profile in Figure 6.12a is applied to the sample. Throughout the performed motion, the dual-stage controlled robotic system actively tracks the sample, with the internal MP position error in motion direction (DoF x) and the translational out-of-plane DoF z shown in Figure 6.12b. Within the measurement interval at the plateau velocity of $v_{sample} = 10\,mm/s$, a tracking error of 486 nm rms in motion direction is achieved (Figure 6.12c). In the translational out-of-plane DoF z, the tracking error is with 167 nm rms even lower. Figure 6.12d shows the performed 3D image within the measurement interval with the entire system in motion. As can be seen, the grating structure as well

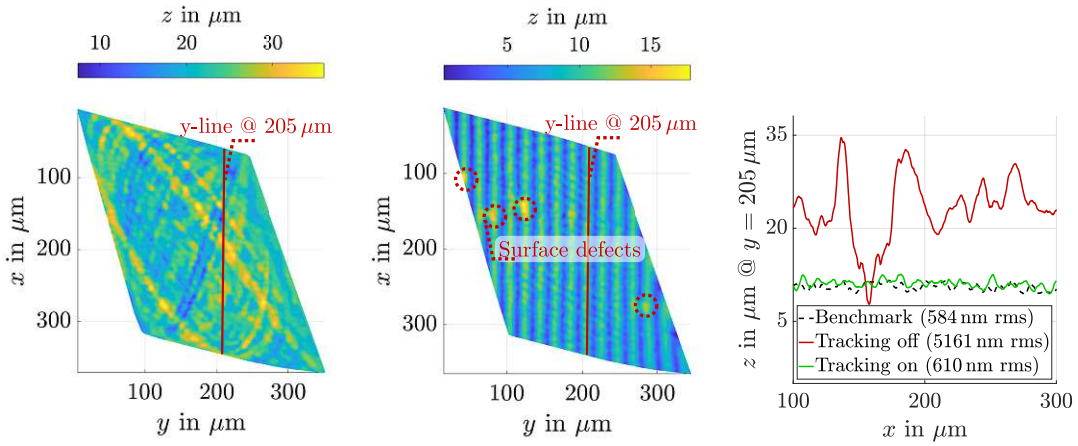

(a) (b) (c)

Figure 6.11: Evaluation of the 3D imaging performance using low and high BW tracking control at a sample velocity of 1 mm/s. (a) shows the measured sample structure with low BW tracking control by repositioning the IR's TCP solely by the knowledge of the conveyor velocity. The measured sample structure for high BW tracking control and the dual stage-controlled repositioning of the IR's TCP in combination with the feedforward of the conveyor velocity, is illustrated in (b). In (c), the resulting cross-section rms values at $y = 205\,\mu m$ are compared. As can be seen the axial resolution using high BW tracking control is improved by a factor of 9 and allows to measure sample structures on the sub-micrometre scale.

as the surface defects are clearly visible. By again analysing the cross section at $y = 205\,\mu m$, the resulting z-ripple is with 621 nm rms in the same order of magnitude as the one obtained in the static, benchmark case.
In summary, the experimental results demonstrate the capability of the dual stage-controlled robotic system to perform 3D measurements with sub-micrometre precision on moving objects with speeds of up to 10 mm/s.

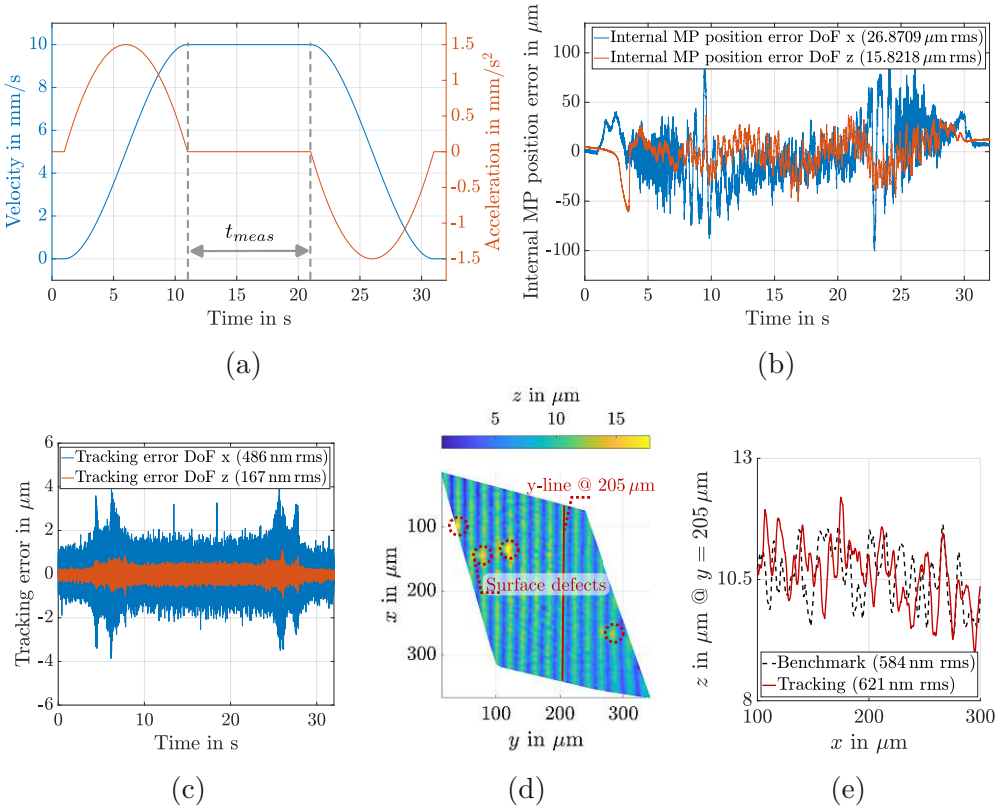

Figure 6.12: Robotic precision 3D measurements on a moving sample at a conveyor velocity of 10 mm/s. (a) shows the applied velocity and acceleration trajectory to the conveyor system with $v_{sample} = 10\,\text{mm/s}$. The performed MP motion in DoF x (motion direction) and DoF z are illustrated in (b). Residual tracking errors for the motion direction (DoF x) and the out-of-plane DoF z of 486 nm rms and 167 nm rms are obtained (c). The measured sample structure is shown in (d). The cross-section rms values at $y = 205\,\mu\text{m}$ with active tracking are in the same order of magnitude compared to the benchmark measurement (d).

6.5 Discussion of the experimental results

In this section, the results acquired within the performance evaluation of the dual stage-controlled robotic system for inline 3D measurements on moving objects are shortly summarized and discussed.

In a first step, the performance of the IR repositioned solely by feedback control is evaluated. The analysis shows that sample velocities of up to 4 mm/s are robustly tracked. However, a rather long acceleration time of 50 s is required, yielding a maximum sample acceleration of $0.12\,\text{mm/s}^2$, which may not be sufficient

considering the demanded efficiency of inline measurement systems.

To increase the system's long-range sample tracking performance, the *a priori* knowledge of the conveyor velocity is integrated in a feedforward approach into the IR repositioning control. The experimental results show that the maximum sample acceleration is increased by a factor of 62, while a sample motion with a velocity of up to 10 mm/s is robustly tracked by the dual stage-controlled robotic system.

With the sample being moved with a constant velocity of 10 mm/s, the residual tracking errors are analysed in a next step. In motion direction (DoF x) and the out-of-plane DoF z, residual tracking errors of 486 nm rms and 167 nm rms are achieved, while actively compensating more than 97 % of disturbing relative motion.

Finally, the system's 3D imaging performance on moving objects is evaluated. Compared to state-of-the-art approach without active sample tracking and repositioning the IR solely by the knowledge of the conveyor velocity, the 3D imaging performance is boosted by a factor of 9 to sub-micrometre precision. At a sample velocity v_{sample} of 10 mm/s, 3D measurements with resolutions down to 621 nm rms are achieved, which is in the same order of magnitude compared to the result obatined by the benchmark measurement (584 nm rms) in static, lab-like conditions.

CHAPTER 7

Conclusion and Outlook

This chapter provides a summary of the overall findings and discusses the achieved system performance as well as its limitations. Finally, this thesis is concluded by an outlook of potential future work to further improve the system performance.

7.1 Conclusion

In this thesis, a dual stage-controlled robotic system for precision inline 3D measurements on moving objects has been successfully designed and evaluated in an industrial-like environment. Aiming to meet the system requirements defined in Section 1.2, a real-time communication interface has been implemented, enabling the desired communication between the state-of-the-art 3D measurement module and the IR control unit. A conveyor system to precisely accelerate and move the sample under test and to emulate an industrial-like environment has been developed. Based on the identified IR dynamics in each DoF, a robust IR repositioning control has been designed in a loop-shaping approach. To enable the long-range tracking of a sample moved by the conveyor system, single input single output (SISO) feedback controllers has been synthesized for each DoF. Using these controllers, the IR is precisely repositioned, maintaining the MP within its limited actuation range.
As the conveyor velocity of an industrial conveyor system is typically known, an additional feedforward control has been designed and included in the control design to further boost the long-range tracking performance. With the targeted application of performing inline 3D measurements on moving objects on the sub-micrometre scale directly in a vibration-prone industrial environment, the achieved performance

of the designed IR repositioning control, the tracking performance of the MP as well as the achieved 3D imaging performance have been separately evaluated in various experiments.

Two research questions arose from studying the state-of-the-art and have been formulated in Section 2.4. In order to conclude the outcomes of this work each question is answered separately.

Research question 1:
Is it feasible to design a dual stage-controlled robotic system for inline measurement applications with sub-micrometre positioning precision and can the system performance be increased by *a priori* knowledge of the conveyor velocity?

Yes, in contrast to the state-of-the-art approach without active sample tracking, the experimental results clearly demonstrate the capability of the dual stage-controlled robotic system to actively track a moving sample with residual tracking errors on the sub-micrometre scale. In the sample motion direction, a residual tracking error of 486 nm rms at a sample velocity of 10 mm/s is achieved, actively compensating about 97 % of the disturbing relative between the measurement tool (MT) and the sample. In the out-of-plane DoF z, the tracking error is with 167 nm rms even lower, highlighting the sub-micrometre positioning precision of the dual stage-controlled robotic system.
By including the information of the conveyor velocity into the IR repositioning control by means of a feedforward approach, sample motions up to 10 mm/s can be robustly tracked, leading to experimental obtained maximum sample accelerations of 7.5 mm/s^2, which is a performance increase by a factor of more than 60 compared to the purely feedback-controlled system.

Research question 2:
Is it feasible to perform robotic 3D measurements with sub-micrometre precision on a moving object?

Yes, using the integrated SCCS to obtain precision 3D measurements within a measurement time of 10 s, a 3D imaging performance on a moving sample in sub-micrometre precision is enabled. The measurement results clearly highlight the system's capability of detecting sample surface defects with the sample being in motion, which is highly demanded for the 100 % control of future industrial manufacturing systems. Surface defects with a lateral dimension of 10 µm and less have been successfully measured at a sample speed of 10mm/s. With the sample continuously moving at the maximum velocity of 10mm/s, precision 3D measure-

ments on a defined grating structure with resolutions down to 621 nm rms have been achieved. This performance is in the same order of magnitude as obtained in the benchmark measurement on the non-moving, static sample. Hence, the sample tracking control-induced stiff link between the MT and the moving sample enables robotic 3D measurements with sub-micrometre precision on moving objects.

7.2 Outlook

Aiming to further increase the system performance with respect to higher sample velocities and the inspection of sample surfaces in arbitrary robot poses, the most limiting factor of the designed system is highlighted.

The selected real-time communication interface KUKA Robot Sensor Interface (RSI) allows to reposition the IR's TCP solely on relative or absolute position correction values, which drastically restricts the control design. The identified time delay as well as the overall, non-constant time of several seconds needed to perform applied position corrections require additional control strategies, which avoid the queuing of cyclically applied corrections and the resulting unfavourable control behaviour as well as IR repositioning. With an eye towards the targeted application, it is recommended to use an IR, whose control can be integrated into the overall, holistic system design, enabling more sophisticated motion control architectures by having full access to the IR parameters.

Bibliography

[1] H. Lasi, P. Fettke, H.-G. Kemper, T. Feld, and M. Hoffmann, "Industry 4.0," *Business & information systems engineering*, vol. 6, no. 4, pp. 239–242, 2014.

[2] D. Imkamp, J. Berthold, M. Heizmann, K. Kniel, M. Peterek, R. Schmitt, J. Seidler, and K.-D. Sommer, "Herausforderungen und Trends in der Fertigungsmesstechnik – Industrie 4.0," *tm - Technisches Messen*, vol. 83, no. 7-8, pp. 417–429, 2016.

[3] K.-S. Wang, "Towards zero-defect manufacturing (ZDM) – a data mining approach," *Advances in Manufacturing*, vol. 1, no. 1, pp. 62–74, 2013.

[4] VDI Verein Deutscher Ingenieure e.V., *VDI/VDE-Gesellschaft Mess- und Automatisierungstechnik (GMA) Herausgeber: Fertigungsmesstechnik 2020, Technologie-Roadmap für die Messtechnik in der industriellen Produktion.* Düsseldorf: Düsseldorf : VDI/VDE-Gsellschaft Mess- und Automatisierungstechnik, 2011.

[5] G. Lanza, B. Haefner, L. Schild, D. Berger, N. Eschner, R. Wagner, and M. Zaiss, "In-Line measurement technology and quality control," in *Metrology*, ser. Precision Manufacturing, Singapore: Springer Singapore, 2019, pp. 399–433.

[6] A. Yogeswaran and P. Payeur, "3D surface analysis for automated detection of deformations on automotive body panels," in *New Advances in Vehicular Technology and Automotive Engineering*, J. P. Carmo and J. E. Ribeiro, Eds., Rijeka: IntechOpen, 2012, ch. 12.

[7] T.-F. Yao, A. Duenner, and M. Cullinan, "In-Line dimensional metrology in nanomanufacturing systems enabled by a passive semiconductor wafer alignment mechanism," *Journal of Micro and Nano-Manufacturing*, vol. 5, no. 1, Nov. 2016.

[8] G. Sansoni, M. Trebeschi, and F. Docchio, "State-of-the-art and applications of 3D imaging sensors in industry, cultural heritage, medicine, and criminal investigation," *Sensors*, vol. 9, no. 1, pp. 568–601, 2009.

[9] H. Schwenke, U. Neuschaefer-Rube, T. Pfeifer, and H. Kunzmann, "Optical methods for dimensional metrology in production engineering," *CIRP Annals*, vol. 51, no. 2, pp. 685–699, 2002.

[10] Y. Wen, J. Hu, and P. R. Pagilla, "A novel robotic system for finishing of freeform surfaces," in *2019 International Conference on Robotics and Automation (ICRA)*, 2019, pp. 5571–5577.

[11] E. Savio, L. De Chiffre, and R. Schmitt, "Metrology of freeform shaped parts," *CIRP Annals*, vol. 56, no. 2, pp. 810–835, 2007.

[12] Y. Zhao, J. Zhao, L. Zhang, and L. Qi, "Development of a robotic 3D scanning system for reverse engineering of freeform part," in *2008 International Conference on Advanced Computer Theory and Engineering*, 2008, pp. 246–250.

[13] U. Schneider, M. Drust, M. Ansaloni, C. Lehmann, M. Pellicciari, F. Leali, J. W. Gunnink, and A. Verl, "Improving robotic machining accuracy through experimental error investigation and modular compensation," *International Journal of Advanced Manufacturing Technology*, vol. 85, no. 1-4, pp. 3–15, 2014.

[14] E. Csencsics, M. Thier, S. Ito, and G. Schitter, "Supplemental peak filters for advanced disturbance rejection on a high precision endeffector for robot-based inline metrology," *IEEE/ASME Transactions on Mechatronics*, p. 1, 2021.

[15] R. Saathof, M. Thier, R. Hainisch, and G. Schitter, "Integrated system and control design of a one DoF nano-metrology platform," *Mechatronics*, vol. 47, pp. 88–96, 2017.

[16] S. Verma, Won-jong Kim, and Jie Gu, "Six-axis nanopositioning device with precision magnetic levitation technology," *IEEE/ASME Transactions on Mechatronics*, vol. 9, no. 2, pp. 384–391, 2004.

[17] H. Zhu, T. J. Teo, and C. K. Pang, "Design and modeling of a six-degree-of-freedom magnetically levitated positioner using square coils and 1-D Halbach arrays," *IEEE Transactions on Industrial Electronics*, vol. 64, no. 1, pp. 440–450, 2017.

[18] Z. Gong, L. Ding, H. Gao, H. Yue, R. Liu, and Z. Deng, "Design and control of a novel six-DoF maglev platform for positioning and vibration isolation," in *2017 2nd International Conference on Advanced Robotics and Mechatronics (ICARM)*, 2017, pp. 155–160.

[19] D. Wertjanz, E. Csencsics, J. Schlarp, and G. Schitter, "Design and control of a MAGLEV platform for positioning in arbitrary orientations," in *2020 IEEE/ASME International Conference on Advanced Intelligent Mechatronics (AIM)*, 2020, pp. 1935–1942.

[20] D. Wertjanz, E. Csencsics, T. Kern, and G. Schitter, "Bringing the lab to the fab: Robot-based inline measurement system for precise 3-D surface inspection in vibrational environments," *IEEE Transactions on Industrial Electronics*, vol. 69, no. 10, pp. 10 666–10 673, 2022.

[21] R. M. Schmidt, G. Schitter, A. Rankers, and J. van Ejik, *The Design of High Performance Mechatronics: High-Tech Functionality by Multidisciplinary System Integration*, 2., rev. ed. Delft: Delft Univ. Press, 2014.

[22] H. Kihlman, R. Loser, A. Cooke, A. Sunnanbo, and K. von Arb, "Metrology-integrated industrial robots: calibration, implementation and testing," in *35th ISR International Symposium on Robotics, 23-26 March, Paris, France*, 2004.

[23] K. SangJoo, C. Wan Kyun, and Y. Youngil, "On the coarse/fine dual-stage manipulators with robust perturbation compensator," in *Proceedings 2001 IEEE International Conference on Robotics and Automation (ICRA.)*, vol. 1, 2001, pp. 121–126.

[24] A.T. Elfizy, G.M. Bone, and M.A. Elbestawi, "Design and control of a dual-stage feed drive," *International Journal of Machine Tools and Manufacture*, vol. 45, no. 2, pp. 153–165, 2005.

[25] S. Ito, J. Steininger, and G. Schitter, "Low-stiffness dual stage actuator for long rage positioning with nanometer resolution," *Mechatronics*, vol. 29, pp. 46–56, 2015.

[26] E. Kiraci, P. Franciosa, G. A. Turley, A. Olifent, A. Attridge, and M. A. Williams, "Moving towards in-line metrology: evaluation of a Laser Radar system for in-line dimensional inspection for automotive assembly systems," *The International Journal of Advanced Manufacturing Technology*, vol. 91, no. 1-4, pp. 69–78, 2016.

[27] D. Imkamp, R. Schmitt, and J. Berthold, "Blick in die Zukunft der Fertigungsmesstechnik," vol. 79, no. 10, pp. 433–439, 2012.

[28] Y. Li and P. Gu, "Free-form surface inspection techniques state of the art review," *Computer-Aided Design*, vol. 36, no. 13, pp. 1395–1417, 2004.

[29] S. Lemes, D. Strbac, and M. Cabaravdic, "Using industrial robots to manipulate the measured object in CMM," *International Journal of Advanced Robotic Systems*, vol. 10, no. 7, p. 281, 2013.

[30] E. Csencsics, S. Ito, J. Schlarp, M. Thier, and G. Schitter, "Hochpräzise roboterbasierte 3D-In-Prozess-Messtechnik," *Elektrotechnik und Informationstechnik*, vol. 135, no. 6, pp. 382–388, 2018.

[31] Carl Zeiss Industrielle Messtechnik Austria GmbH, *ZEISS ABIS; Surface Inspection; Efficient. Objective. Fatigue-free*, `https://www.zeiss.at/messtechnik/produkte/systeme/optical-measurement/3d-digitalisierung/zeiss-abis-ii.html#brochuredownload`, Accessed: 10.05.2022.

[32] G. B. de Sousa, A. Olabi, J. Palos, and O. Gibaru, "3D metrology using a collaborative robot with a laser triangulation sensor," *Procedia Manufacturing*, vol. 11, pp. 132–140, 2017.

[33] S. Yin, Y. Ren, Y. Guo, J. Zhu, S. Yang, and S. Ye, "Development and calibration of an integrated 3D scanning system for high-accuracy large-scale metrology," *Measurement*, vol. 54, pp. 65–76, 2014.

[34] P. Besset, A. Olabi, and O. Gibaru, "Advanced calibration applied to a collaborative robot," in *2016 IEEE International Power Electronics and Motion Control Conference (PEMC)*, 2016, pp. 662–667.

[35] F. Sherwani, M. M. Asad, and B. Ibrahim, "Collaborative robots and industrial revolution 4.0 (IR 4.0)," in *2020 International Conference on Emerging Trends in Smart Technologies (ICETST)*, 2020, pp. 1–5.

[36] B. Greenway, "Robot accuracy," *Industrial Robot*, vol. 27, no. 4, pp. 257–265, 2000.

[37] Z. Roth, B. Mooring, and B. Ravani, "An overview of robot calibration," *IEEE Journal on Robotics and Automation*, vol. 3, no. 5, pp. 377–385, 1987.

[38] J. H. Jang, S. H. Kim, and Y. K. Kwak, "Calibration of geometric and non-geometric errors of an industrial robot," *Robotica*, vol. 19, no. 3, pp. 311–321, 2001.

[39] D. E. Whitney, C. A. Lozinski, and J. M. Rourke, "Industrial robot forward calibration method and results," *Journal of Dynamic Systems, Measurement, and Control*, vol. 108, no. 1, pp. 1–8, Mar. 1986.

[40] Thorlabs, Inc., *Sources of Vibration*, `https://www.thorlabs.com/newgrouppage9.cfm?objectgroup_id=8275`, Accessed: 06.04.2022.

[41] C. G. Gordon, "Generic criteria for vibration-sensitive equipment," in *Vibration Control in Microelectronics, Optics, and Metrology*, Colin G. Gordon, Ed., vol. 1619, SPIE, 1992, pp. 71–85.

[42] C. Connolly, "Vibration isolation theory and practice," *Assembly Automation*, vol. 29, no. 1, pp. 8–13, 2009.

[43] R.A. Ibrahim, "Recent advances in nonlinear passive vibration isolators," *Journal of Sound and Vibration*, vol. 314, no. 3, pp. 371–452, 2008.

[44] R. G. Cobb, J. M. Sullivan, A. Das, L. P. Davis, T. T. Hyde, T. Davis, Z. Rahman, and J. T. Spanos, "Vibration isolation and suppression system for precision payloads in space," *Smart Materials and Structures*, vol. 8, no. 6, pp. 798–812, 1999.

[45] R. L. Hollis and S. E. Salcudean, *Lorentz Levitation Technology: a New Approach to Fine Motion Robotics, Teleoperation, Haptic Interfaces, and Vibration Isolation*. Citeseer, 1993.

[46] L. Kramer, T. van den Dool, and G. Witvoet, "Demonstrator for nano-precision multi-agent MAGLEV positioning platform for high throughput metrology," *IFAC-PapersOnLine*, vol. 52, no. 15, pp. 471–476, 2019.

[47] M. Thier, R. Saathof, A. Sinn, R. Hainisch, and G. Schitter, "Six degree of freedom vibration isolation platform for in-line nano-metrology," *IFAC-PapersOnLine*, vol. 49, no. 21, pp. 149–156, 2016.

[48] D. Wertjanz, E. Csencsics, and G. Schitter, "Three-DoF vibration compensation platform for robot-based precision inline measurements on free-form surfaces," *IEEE Transactions on Industrial Electronics*, vol. 69, no. 1, pp. 613–621, 2022.

[49] L. Guo, D. Martin, and D. Brunnett, "Dual-stage actuator servo control for high density disk drives," in *1999 IEEE/ASME International Conference on Advanced Intelligent Mechatronics*, 1999, pp. 132–137.

[50] C. Knospe, "PID control," *IEEE Control Systems Magazine*, vol. 26, no. 1, pp. 30–31, 2006.

[51] K.J. Åström and T. Hägglund, "The future of PID control," *Control Engineering Practice*, vol. 9, no. 11, pp. 1163–1175, 2001.

[52] R. P. Borase, D. K. Maghade, S. Y. Sondkar, and S. N. Pawar, "A review of PID control, tuning methods and applications," *International Journal of Dynamics and Control*, vol. 9, no. 2, pp. 818–827, 2020.

[53] Y. Li, K. Heong Ang, and G. Chong, "PID control system analysis and design," *IEEE Control Systems Magazine*, vol. 26, no. 1, pp. 32–41, 2006.

[54] S. W. Sung, J. Lee, and I.-B. Lee, *Process Identification and PID Control*, 1. Aufl. Hoboken, N.J: Wiley-IEEE Press, 2009.

[55] L. Wang, *PID Control System Design and Automatic Tuning using MATLAB/Simulink*, 1st ed. Newark: Wiley, 2020.

[56] J. G. Ziegler and N. B. Nichols, "Optimum settings for automatic controllers," *Journal of Dynamic Systems, Measurement, and Control*, vol. 115, no. 2 B, pp. 220–222, 1993.

[57] K.J. Åström and T. Hägglund, "Revisiting the ziegler–nichols step response method for PID control," *Journal of Process Control*, vol. 14, no. 6, pp. 635–650, 2004.

[58] F. K. Zadeh, P. Moallem, S. Asiri, and M. M. Zadeh, "LQR motion control and analysis of a prototype spherical robot," in *2014 Second RSI/ISM International Conference on Robotics and Mechatronics (ICRoM)*, 2014, pp. 890–895.

[59] M. H. Yaseen and H. J. Abd, "Modeling and control for a magnetic levitation system based on SIMLAB platform in real time," *Results in Physics*, vol. 8, pp. 153–159, 2018.

[60] Y. Sam, M. Ghani, and N. Ahmad, "LQR controller for active car suspension," in *2000 TENCON Proceedings. Intelligent Systems and Technologies for the New Millennium*, vol. 1, 2000, pp. 441–444.

[61] L. Liu, S. Tian, D. Xue, T. Zhang, and Y. Chen, "Industrial feedforward control technology: a review," *Journal of Intelligent Manufacturing*, vol. 30, no. 8, pp. 2819–2833, 2018.

[62] C. Lo Bianco, A. Tonielli, and R. Zanasi, "Nonlinear trajectory generator for evolution control systems," in *Proceedings of the 1996 IEEE IECON. 22nd International Conference on Industrial Electronics, Control, and Instrumentation*, vol. 1, 1996, pp. 195–201.

[63] D. Wertjanz, T. Kern, A. Pechhacker, E. Csencsics, and G. Schitter, "Robotic precision 3D measurements in vibration-prone environments enabled by active six dof sample-tracking (accepted)," *IEEE Transactions on Industrial Electronics*, 2022.

[64] D. Wertjanz, T. Kern, E. Csencsics, G. Stadler, and G. Schitter, "Compact scanning confocal chromatic sensor enabling precision 3-D measurements," *Applied Optics*, vol. 60, no. 25, pp. 7511–7517, Sep. 2021.

[65] D. Wertjanz, E. Csencsics, and G. Schitter, "An efficient control transition scheme between stabilization and tracking task of a MAGLEV platform enabling active vibration compensation," in *2020 IEEE/ASME International Conference on Advanced Intelligent Mechatronics (AIM)*, 2020, pp. 1943–1948.

[66] KUKA Deutschland GmbH, *Robots KR Agilus-2 Montageanleitung*, `https://xpert.kuka.com/service-express/portal/project1_p/document/kuka-project1_p-basic_AR23943_de?context=%7B%7D`, Accessed: 19.04.2022.

[67] KUKA Deutschland GmbH, *KUKA.RobotSensorInterface 4.1*, `https://xpert.kuka.com/service-express/portal/project1_p/document/kuka-project1_p-common_PB11890_de?context=%7B%7D`, Accessed: 05.05.2022.

[68] KUKA Deutschland GmbH, *KUKA.EtherCAT Bridge für KR C4*, `https://xpert.kuka.com/service-express/portal/project1_p/document/kuka-project1_p-common_PB3158_de?context=%7B"filter"%3A%7B%7D,"text"%3A"ethercat%20bridge","page"%3A1,"useExpertQuery"%3A0%7D`, Accessed: 05.05.2022.

[69] International Electrotechnical Commission, *IEC 61131 – Programmable controllers, Part 3: Programming languages*, 2013.

[70] A. Karim, J. Hitzer, A. Lechler, and A. Verl, "Analysis of the dynamic behavior of a six-axis industrial robot within the entire workspace in respect of machining tasks," in *2017 IEEE International Conference on Advanced Intelligent Mechatronics (AIM)*, 2017, pp. 670–675.

[71] N. Sclater, *Mechanisms and Mechanical Devices Sourcebook*. McGraw-Hill Education, 2011.

[72] F. Ghorbel, J. Hung, and M. Spong, "Adaptive control of flexible-joint manipulators," *IEEE Control Systems Magazine*, vol. 9, no. 7, pp. 9–13, 1989.

[73] M. Chan, "Controller Synthesis and Vibration Suppression Techniques for Industrial Robotic Manipulators with Joint Flexibilities," Ph.D. dissertation, 2013.

Eigenständigkeitserklärung

Hiermit erkläre ich, dass die vorliegende Arbeit gemäß dem Code of Conduct, insbesondere ohne unzulässige Hilfe Dritter und ohne Benutzung anderer als der angegebenen Hilfsmittel, angefertigt wurde. Die aus anderen Quellen direkt oder indirekt übernommenen Daten und Konzepte sind unter Angabe der Quelle gekennzeichnet.

Die Arbeit wurde bisher weder im In- noch im Ausland in gleicher oder ähnlicher Form in anderen Prüfungsverfahren vorgelegt.

Wien, im Juli 2022

Matthias Laimer, BSc.